# UNDEREXPANDED SUPERSONIC PLUME SURFACE INTERACTIONS: APPLICATIONS FOR SPACECRAFT LANDINGS ON PLANETARY BODIES

M. Mehta[1]
Aerosciences Branch, EV33
NASA Marshall Space Flight Center
Huntsville, AL

A. Sengupta[2]
EDL and Advanced Technologies Division, 313H
NASA Jet Propulsion Laboratory
California Institute of Technology
Pasadena, CA

N. O. Renno[3]
Department of Atmospheric and Space Sciences
University of Michigan
Ann Arbor, MI

J. W. Van Norman[4]
Analytical Mechanical Associates, Inc.
Atmospheric Flight and Entry Systems Branch, D205
NASA Langley Research Center
Hampton, VA

P. G. Huseman[5] and D. S. Gulick[6]
Orion Aerosciences Division
Lockheed Martin Space Systems
Denver, CO

## NOMENCLATURE

Variables

| | | |
|---|---|---|
| $\rho$ | = | jet or rocket plume density (kg/m$^3$) |
| $t$ | = | time (s) |
| $f$ | = | engine pulse frequency (Hz) |
| $P$ | = | pressure (Pa) |
| $\tau$ | = | shear stress |
| $c_p$ | = | jet or plume specific heat capacity at constant pressure |
| $\lambda$ | = | jet or plume thermal conductivity |
| $T$ | = | temperature (K) |
| $\beta$ | = | jet or plume coefficient of thermal expansion |
| $\varphi$ | = | rate of viscous dissipation |
| $x$ | = | axial length along the jet/plume axis (m) |
| $D$ | = | diameter (m) |
| $U$ | = | plume or jet velocity (m/s) |
| $\mu$ | = | plume or jet viscosity (Pa-s) |
| $g$ | = | gravitational acceleration (m/s$^2$) |
| $\gamma$ | = | specific heat ratio of exhaust plume |
| $c_v$ | = | specific heat capacity at constant volume |

---

[1] Aerospace Engineer, EV33/NASA MSFC, AIAA Member
[2] Aerospace Engineer, MS 301-490, AIAA Member
[3] Professor, AIAA Member
[4] Aerospace Engineer, MS 489, AIAA Member
[5] Aerospace Engineer/Manager, AIAA Associate Fellow
[6] Aerospace Engineer, AIAA Member

$R$ = gas constant (J/K-mol)
$F$ = force (N)
$A$ = nozzle cross-sectional area ($m^2$)
$m$ = jet mass flow rate (kg/s)

Subscripts

e = nozzle exit conditions
∞ = ambient conditions
fb = free boundary conditions
* = solid surface boundary conditions
t = total

## ABSTRACT

Numerical and experimental investigations of both far-field and near-field supersonic steady jet interactions with a flat surface at various atmospheric pressures are presented in this paper. These studies were done in assessing the landing hazards of both the NASA Mars Science Laboratory and Phoenix Mars spacecrafts. Temporal and spatial ground pressure measurements in conjunction with numerical solutions at altitudes of ~35 nozzle exit diameters and jet expansion ratios (e) between 0.02 and 100 are used. Data from steady nitrogen jets are compared to both pulsed jets and rocket exhaust plumes at Mach ~5. Due to engine cycling, overpressures and the plate shock dynamics are different between pulsed and steady supersonic impinging jets. In contrast to highly over-expanded (e <1) and underexpanded exhaust plumes, results show that there is a relative ground pressure load maximum for moderately underexpanded (e ~2-5) jets which demonstrate a long collimated plume shock structure. For plumes with e >>5 (lunar atmospheric regime), the ground pressure is minimal due to the development of a highly expansive shock structure. We show this is dependent on the stability of the plate shock, the length of the supersonic core and plume decay due to shear layer instability which are all a function of the jet expansion ratio. Asymmetry and large gradients in the spatial ground pressure profile and large transient overpressures are predominantly linked to the dynamics of the plate shock. More importantly, this study shows that thruster plumes exhausting into martian environments possess the largest surface pressure loads and can occur at high spacecraft altitudes in contrast to the jet interactions at terrestrial and lunar atmospheres. Theoretical and analytical results also show that subscale supersonic cold gas jets adequately simulate the flow field and loads due to rocket plume impingement provided important scaling parameters are in agreement. These studies indicate the critical importance of testing and modeling plume-surface interactions for descent and ascent of spacecraft and launch vehicles.

## INTRODUCTION

Supersonic jet interactions with the ground or flat surface are a complex fluid dynamics problem with many nonlinearities. These nonlinearities arise from shock-wave surface interactions, stagnation bubble formation and the propagation of wall jets along the surface. Lamont and Hunt [1980][1] studied the flow field and surface interactions due to axisymmetric underexpanded supersonic nitrogen jets at distances between one and three nozzle exit diameters. Steady state numerical simulations, conducted by Fujii et al [2002][2] at these distances, show good agreement with Lamont and Hunt's experimental results. Most of literature concentrates on studies where the nozzle pressure ratios (NPR) are below 10[1,3]. NPR is the ratio of nozzle chamber pressure to ambient pressure.

By applying Schlieren imaging and ground pressure sensors along with numerical simulations, important flow structures such as the plate shock and stagnation bubble were identified. A plate shock is a reflected and detached shock wave from a surface due to the impingement of a supersonic jet[1] and this is observed in many applications such as solar wind forming a curved bow shock reflection from the Earth's surface[4] to a planar bow shock formed during an Apollo capsule reentry into the Earth's atmosphere[5]. Stagnation bubble (recirculation zones) can form below the plate shock and has only recently received more attention due to its effects on acoustic noise production[6,7]. The third structure of importance is the propagating wall jet which can reach supersonic speeds, demonstrate compression and expansion regimes and decay as a function of axial distance from the impingement point[7]. These flow

features are within the far-field or shock wave interaction regime, and are considerably different than the flow structures observed in the near-field regime.

The near-field regime is within the first nozzle exit diameter from the nozzle exit plane. Near-field supersonic jet characteristics are dependent on the nozzle chamber stagnation pressure, nozzle area ratio and atmospheric pressure. There are three types of flow characteristics which are first observed at this regime: overexpansion, underexpansion and perfect expansion of the jet[8]. All three flow characteristics are observed when rockets launch into space and as discussed in this paper lead to different far-field surface interactions.

The main focus of this study is to investigate the flow physics of plume ground interactions from exhaust plumes of rocket motor engines during planetary landings, specifically for environments of Mars. For appropriate simulations, this requires different flow requirements than observed for past studies conducted by Lamont and Hunt[1], Krothapalli et al[9], Henderson et al.[6] and other researchers focused on the acoustic nature of impinging jets. Rocket plumes exhausting into near-vacuum planetary environments demonstrate higher exit Mach numbers on the order Mach ~5 with nozzle pressure ratios greater than 1000, an order three times larger in magnitude for those observed in acoustic studies[9]. Rocket plumes interact with the surface at much higher altitudes between ~100$d$ and ~5$d$, where $d$ is the nozzle exit diameter[10], to decelerate the spacecraft and to ensure a successful soft landing. In contrast to previous studies, all of our tests were conducted at reduced atmospheric pressures which spanned from the martian to terrestrial environments. The largest difference between previous jet impingement studies is the engine mode can be either pulsed or steady during landings and attitude corrections. Comparative studies between these two modes are limited.

This paper will look at numerical and experimental ground interaction data between pulsed and steady underexpanded supersonic jets exhausting from simulated Phoenix Rocket Engine Module (REM) and Mars Science Laboratory Main Landing Engine (MLE) nozzles. More importantly, we will focus on these interactions associated with jets exhausting from high altitudes of $h > 20d$. We will then compare our experimental sub-scale temporal and spatial results with numerical simulations at both subscale and full-scale to provide further insight in the complex flow physics and to ascertain the reliability of our scaling laws. This study was performed to reduce mission risk for both of NASA's recent Mars missions.

## ROCKET PLUME STRUCTURE IN VARIOUS ATMOSPHERIC ENVIRONMENTS

Plume-surface flow physics in tenuous to vacuum atmospheres due to steady supersonic jets have been studied by researchers in preparation for the Apollo missions[11]. The main methods of characterizing these flows are to spatially and temporally determine the pressure fields and density gradients. There are three types of supersonic free-jets that exhaust from nozzles. The jet or rocket plume can either be underexpanded, overexpanded or perfectly expanded[12]. The jet pressure tries to match the ambient pressure which leads to large differences in their shock structure.

For an underexpanded jet, the exit jet pressure ($P_n$) is larger than the ambient ($P_b$) and this leads to Prandtl-Meyer (PM) expansion waves, initiated at the lip of the nozzle (shown as blue lines in Figure 1A1), which reduces the jet pressure to match the ambient. Due to reflection of the PM expansion waves in region 2 shaded in grey, this leads to a jet pressure smaller than the ambient in region 3. Hence, this results in the reflection of these expansion waves from the ambient boundary, resulting in PM compression waves. The coalescing of the compression waves leads to oblique shocks shown as red lines. This results in the matching of the two competing pressures in region 4. When oblique shock reflection occurs, the jet pressure is larger than ambient in region 5 and the process starts again. These are known as "shock cells" which form as repeatable train-like structures as shown in Figure 1A1. They dissipate further downstream due to viscous losses and turbulent mixing with the ambient atmosphere. We show a planar-laser-induced-fluorescence (PLIF) spark image in Figure 1A2 and a contour image of the standard deviation of the mean velocity (standard deviation image) in Figure 1A3 of an underexpanded jet[13]. The standard deviation image correlates to turbulence intensity.

For an overexpanded jet, the exit pressure is smaller than the ambient and this leads to the formation of oblique shock waves at the nozzle lip shown in region 1 in Figure 1B1. The same dynamics as for the underexpanded jets are observed, but they are out-of-phase where it is now first compression and then expansion. The PLIF and standard deviation images are shown in Figures 1B2 and 1B3 respectively[13]. Turbulence and unsteadiness are much more pronounced for overexpanded jets which may lead to instability and faster dissipation of the plume structure. According to Hagerman and Frey[14], the diffusion rate of the entrained flow into the turbulent mixing region, the interface region between the jet shock and the ambient atmosphere, is larger than the underexpanded case and increases axially. Due to overexpansion of the plume, the free atmospheric boundary pinches the jet inward, leading to an increase in the turbulent mixing region and attenuation of the inviscid core. For perfectly expanded jet, the criteria for both pressures to be matched are met at the nozzle exit and hence, no expansion or compression waves are observed.

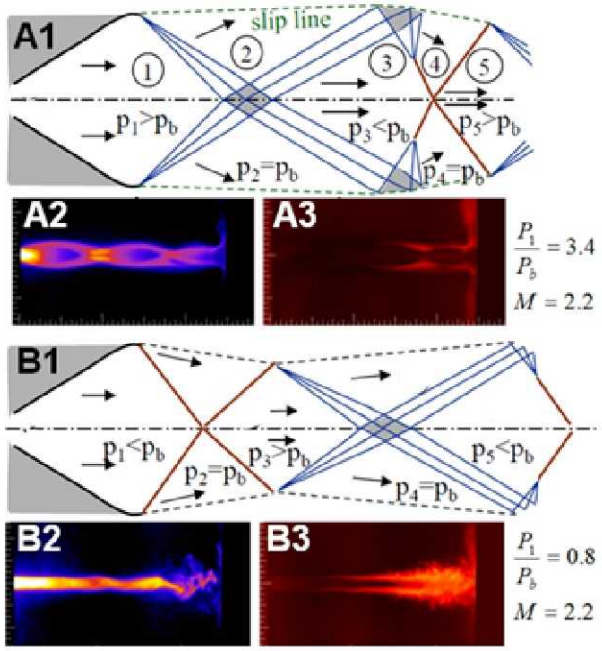


Figure 1. Plume shock structure of underexpanded and overexpanded supersonic jets. (A1) Schematic of an underexpanded supersonic jet. (A2) PLIF spark image and (A3) PLIF standard deviation image[10]. (B1) Schematic of an overexpanded supersonic jet. (B2) PLIF spark image and (B3) PLIF standard deviation image[10].

Most rocket plumes exhausting from a descent engine on Mars or the moon are underexpanded and this classification will be the prime focus of our studies. However, the plume structure and their effects on the surface are considerably different between the two atmospheres. Flow structures due to impinging steady jets were separated into three regimes as discussed by Donaldson and Snedekar [1971][15]: (a) free-jet; (b) impingement zone and (c) wall jet. These structures are mainly characterized by pressure and density fields at steady-state as done by Stitt [1966][16] for preparation of the first landings on the moon. We will briefly discuss the flow structures within the impingement zone and wall jet which are considerably the most important for ground erosion[1]. The plate shock, tail shock and stagnation bubble below the plate shock as shown in Figure 2A are important flow structures which we show directly influences the ground pressure. Tail shocks are oblique shock waves which are reflected from the plate shock and emanate from the triple point. The triple point is the region where the incident, plate and tail shocks converge (Fig. 2A). Since the total pressure loss is much greater for a plate shock than for oblique tail shocks, there is ring of relatively high surface pressure. A portion of the flow below the plate shock cannot overcome these relatively large pressure gradients on the outboard of the plate shock, resulting in the recirculation of gas (stagnation bubble)[6]. For comparison, we depict the schematic and the Schlieren photograph (Fig. 2B) of an underexpanded impinging jet. Past studies predominantly investigated these

structures at steady-state conditions. One of our goals in this paper is to investigate the behavior of these structures in transient conditions.

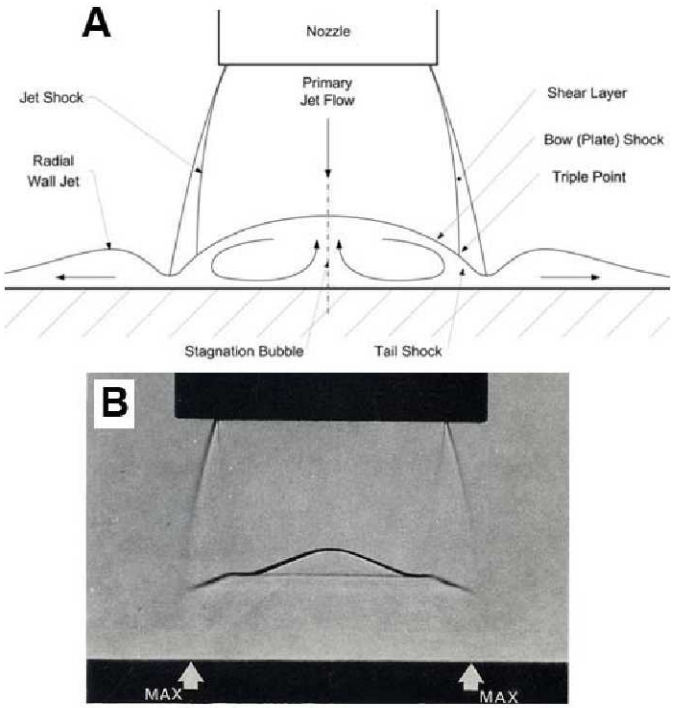


Figure 2. Plume shock structure within the impingement zone of an underexpanded jet. **(**A**)** Schematic of flow structures; (B) Schlieren image distinctly showing a curved plate shock[1]

## SCALING LAWS FOR ROCKET PLUME FLOW PHYSICS

Theoretical scaling laws prove that subscale cold gas jets can simulate the shock structure and ground pressure profiles due to full-scale rocket plume interactions. This is proven through first principles by normalizing the conservation equations. The governing compressible Navier-Stokes equations (Eqns. 1 – 3) are presented in symbolic notation below[17]:

$$\frac{D\rho}{Dt} = -\rho \nabla \cdot \vec{U} \qquad (1)$$

$$\rho \frac{D\vec{U}}{Dt} = \vec{f} - \nabla p + \nabla \cdot [\vec{\tau}] \qquad (2)$$

$$\rho c_p \frac{DT}{Dt} = \nabla \cdot (\lambda \nabla T) + \beta T \frac{Dp}{Dt} + \phi \qquad (3)$$

Where $T$, $p$, $\rho$, $v$, $\lambda$, $\beta$, $c_p$, $\tau$, $t$ and $\phi$ are the plume temperature, pressure, density, velocity, thermal conductivity, coefficient of thermal expansion, isobaric specific heat capacity, the viscous stress tensor, time and the rate of viscous dissipation, respectively. The volumetric force is denoted by $f$. Arrows above the parameter denote that these terms are vectors. These compressible Navier-Stokes equations are normalized with the following parameters[17]:

$$x' = x/D, \quad t' = tU_e/D, \quad \vec{v}' = \vec{u}/U_e, \quad p' = (p - p_e)/\rho_e U_e^{\,2}, \quad T' = T/T_e, \quad \rho' = \rho/\rho_e,$$
$$c_p^{\,\prime} = c_p/c_{pe}, \quad \lambda' = \lambda/\lambda_e, \quad \beta' = \beta/\beta_e, \quad \nabla' = D\nabla, \quad \phi' = \phi D^2/\mu_e U_e^{\,2}, \quad \mu' = \mu/\mu_e \qquad (4)$$

All the reference parameters are taken at the nozzle exit (denoted as a subscript *e*) with a diameter of *D*. The length scale and plume viscosity are denoted by *x* and $\mu$, respectively. Upon substituting the reference parameters (Eqn. 4) into equations 1-3, the normalized Navier-Stokes equations become:

$$\frac{D\rho'}{Dt'} = -\rho' \nabla' \cdot \vec{v}' \qquad (5)$$

$$\rho' \frac{D\vec{v}'}{Dt'} = \frac{1}{\mathrm{Fr}^2}\rho'\vec{g} - \nabla' p' + \frac{1}{\mathrm{Re}}\nabla' \cdot [\vec{\tau}'] \qquad (6)$$

$$\rho' c_p' \frac{DT'}{Dt'} = \frac{1}{\mathrm{Re}\,\mathrm{Pr}}\nabla' \cdot (\lambda' \nabla' T') + \frac{U^2}{c_{pe}T_e}\beta' T' \frac{Dp'}{Dt'} + \frac{U^2}{c_{pe}T_e\,\mathrm{Re}}\phi' \qquad (7)$$

$$\frac{U^2}{c_{pe}T_e} = \mathrm{Ma}^2 \frac{c_e^{\,2}}{c_{pe}T_e} = \mathrm{Ma}^2(\gamma - 1) \qquad (8)$$

The speed of sound at the nozzle exit is denoted by $c_e$. Substitute Eqn. 8 into Eqn. 7 for compressible ideal gas flow and equation 7 becomes:

$$\rho' c_p' \frac{DT'}{Dt'} = \frac{1}{\mathrm{Re}\,\mathrm{Pr}}\nabla' \cdot (\lambda' \nabla' T') + \mathrm{Ma}^2(\gamma - 1)\beta' T' \frac{Dp'}{Dt'} + \frac{\mathrm{Ma}^2(\gamma - 1)}{\mathrm{Re}}\phi' \qquad (9)$$

Where the following nondimensional terms are defined as:

$$\mathrm{Re} = \frac{\rho_e U_e D}{\mu_e}, \quad \mathrm{Fr} = \frac{U_e}{\sqrt{gD}}, \quad \mathrm{Ma} = \frac{U_e}{a_e}, \quad \mathrm{Pr} = \frac{\mu_e c_{pe}}{\lambda_e}, \quad \gamma = \frac{c_{pe}}{c_{ve}} \qquad (10)$$

Hence, the flow physics of the rocket plume/supersonic jet is a function of the Reynolds number (Re), Froude number (Fr), Mach number (Ma), Prandtl number (Pr) and specific heat ratio capacity ($\gamma$). However, simplifications can be made due to the supersonic flow regime. For example as Fr $\rightarrow\infty$, the first term on the right hand side of Eqn. 6 tends to zero. Also as Re $\rightarrow\infty$ and applied to Eqns. 6 and 7, characteristic of supersonic flows, the flow can be considered inviscid. This is valid for supersonic jet interactions in all regions except at the viscous boundary layer. Here viscosity of the jet plays a role especially in determining the heat transfer and thermal boundary layer. However, the ground total pressure has a relatively minor dependence on the jet viscosity for large Reynolds number and this is known as the Barker effect[17,18].

Similar analyses need to be applied to the boundary conditions imposed by these flows. There are two types of surface boundary conditions for this application: (a) free boundary and (b) solid boundary. The free surface boundary is defined as the infinitesimal interface between the exhaust plumes and the ambient atmosphere ($P_\infty$). At this interface region near the nozzle exit, the entrained flow velocity and temperature are assumed continuous to the plume. The solid surface boundary, intuitively, is defined as the solid surface where the jets interact. At the free boundary[17]:

$$p_{fb} = P_\infty = P_{amb} \qquad (11)$$

$$\vec{v}_{fb} = \vec{U}_e \qquad (12)$$

$$T_{fb} = T_e \qquad (13)$$

Substituting equations 11-13 into the normalized parameters shown in equation 4, these parameters become:

$$p'_{fb} = \frac{P_\infty - P_e}{\rho_e U_e^{\,2}} \qquad (14)$$

$$v'_{fb} = 1.0 \qquad (15)$$

$$T'_{fb} = 1.0 \qquad (16)$$

Since the specific heat ratio and the nozzle area expansion ratio are similar for full-scale and subscale systems, the dynamic pressure at the nozzle exit, $\rho_e U_e^{\,2}$, will be similar from isentropic relations provided the stagnation pressure at the nozzle inlet, $P_C$ are matched. The flow approximation is 1-D isentropic at the nozzle exit. By manipulating equation 14, another nondimensional term named the jet expansion ratio (*e*), developed from the boundary conditions, needs to be satisfied:

$$p'_{fb} = \frac{P_\infty - P_e}{\rho_e U_e^{\,2}} = \frac{P_\infty \left[1 - \left(\frac{P_e}{P_\infty}\right)\right]}{\rho_e U_e^{\,2}} = \frac{P_\infty (1 - e)}{\rho_e U_e^{\,2}} \qquad (17)$$

$P_C$ needs to be matched for both full-scale and subscale systems for equation 17 to be satisfied and this is defined as the nozzle pressure ratio (NPR), $\alpha$. $P_{C\text{-max}}$ is defined as the stagnation chamber pressure when maximum engine thrust is reached. The NPR and jet expansion ratio are defined as follows:

$$\alpha = \frac{P_{C-\max}}{P_\infty} \qquad (18)$$

$$e = \frac{P_e}{P_\infty} \qquad (19)$$

The normalized boundary conditions at the solid surface are the following:

$$p'_* = \frac{P_s - P_e}{\rho_e U_e{}^2} \qquad (20)$$

$$T'_* = \frac{T_s}{T_e} \qquad (21)$$

$$v'_* = 0 \qquad (22)$$

The dimensional term, $T_s$, is the surface impingement temperature. *According to the governing Navier-Stokes equations and boundary conditions specific for supersonic jet interactions, there are five nondimensional numbers that need to be satisfied to ensure dynamic similarity:* ***γ*, Ma, Re, *e*, *α*.** From equation 20 and the matching of these required nondimensional numbers, the ground pressure is theoretically simulated. The ground temperature may be calculated from this approach, but its' large dependence on the viscous boundary layer may lead to large uncertainties. Below is a description of each of these parameters.

The specific heat ratio for the gas mixture of hydrazine combustion products at the nozzle exit is not analytically straight-forward to determine. This parameter is numerically calculated throughout the internal nozzle using two-dimensional Method of Characteristics solutions fully coupled with finite-rate kinetics. From these numerical calculations, the specific heat ratio between the rocket plume and $N_2$ are within 3% of agreement as tabulated in Table 2. Using OVERFLOW CFD code, the specific heat ratio throughout the exhaust plume is ~1.4 [19] and hence, nitrogen test gas was used for our experiments.

The exit Mach number between the two flows is matched by simulating the nozzle expansion ratio, nozzle contour profile and the specific heat ratio. This ensures that the compressibility effects are simulated within the plume. This is also confirmed by numerical simulations. The Mach similarity parameter, as derived above, is a function of the exit Mach number and specific heat ratio and is defined as the ratio of the kinetic energy of the plume to the internal energy of the plume at the nozzle exit[20],

$$k = \gamma(\gamma - 1)M^2 \qquad (23)$$

There are four flow regimes determined by the Reynolds number in increasing order: (a) Stokes or creeping (<1), (b) laminar ($10^0$-$10^3$), (c) transition ($10^3$-$10^4$) and (d) turbulent (>$10^4$) flows. For rocket plumes and supersonic jets used in the experiments, the flow is fully-turbulent as shown in Table 2.6.

The other parameter, as derived above, used to scale our CFTB is the jet expansion ratio of the exhaust plume at the nozzle exit. This term has important physical interpretations as well. The pressure force ratio of the rocket plume at the nozzle exit ($F_e$) relative to the atmosphere ($F_\infty$) is important in determining both the jet expansion angle of the plume with respect to the centerline[10] and shock structure of the plume. This parameter described the effects of the ambient atmosphere on the exhaust plume. Its' far-field effects are described in more detail in this paper. This in turn is determined by the ratio of nozzle exit pressure ($P_e$) to ambient pressure ($P_\infty$) [21],

$$e = \frac{F_e}{F_\infty} = \frac{P_e A_e}{P_\infty A_e} = \frac{P_e}{P_\infty}. \qquad (24)$$

The final scaling parameter used is the nozzle pressure ratio (Eqn. 18). NPR is an important parameter in ensuring that the test nozzles have ground pressure profiles similar to the full-scale case of the real size and performance of the rocket motor. Simulation of the thruster plume temperature is not critical in understanding the force loads on the surface[11]. This is further corroborated by normalization of the conservation of energy (Eqn. 9) which is only a function of the Mach similarity parameter for supersonic turbulent flows.

The Strouhal number, which is the ratio of the inertial force associated with unsteady flow characteristics to the inertial force due to the velocity gradient (Eqn. 25). This nondimensional number is applied strictly for pulsed jets[22]. The dimensional quantities used to calculate these scaling parameters are tabulated in Table A2. We will briefly discuss how these various parameters, in particular the jet expansion ratio and Strouhal number, change the flow physics at the far-field/interaction regime.

$$\mathrm{St} = \frac{fD}{U_e} \qquad (25)$$

By matching these nondimensional numbers and the geometric length scaling with respect to the nozzle diameter, the ground pressure profiles and the plume and impingement flow structures produced by the test nozzles theoretically simulates those produced by the rocket exhaust. This is further confirmed by comparing full-scale and subscale numerical analyses as described in this paper. Table 1 quantitatively compares non-dimensional plume parameters between the experimental setup and full-scale. Based on the similarity of the nondimensional parameters shown in Table 1, the subscale tests theoretically simulates the interactions of the Phoenix and MSL rocket plume with the impermeable surface. The rocket exhaust parameters may vary slightly depending on the extent of ammonia disassociation during the hydrazine decomposition reaction.

| | | **MSL MLE** | | **Phoenix REM** | |
|---|---|---|---|---|---|
| | | **¼ scale** | **full-scale** | **½ scale** | **full-scale** |
| Hypersonic similarity | $k$ | 14.8 | 14.0 | 12.7 | 11.4 |
| Jet expansion ratio | $e$ | 2.9 – 2.1 - exp<br>3.5 - num | 6.8 – 2.2 – flt<br>6.8 – 4.1 - num | ~4.4 - exp<br>4.5 – num | 3.8 - flt<br>4.7 – num |
| Reynolds Number | $Re$ | 24.5 – 14.7 x $10^5$ -exp<br>23.3 x $10^5$ - num | 8.4 – 5.0 x $10^5$ - flt | 12.7 x $10^5$ | 3.4 x $10^5$ |
| Mach Number | $M_e$ | 5.14 | 5.08 | 4.77 | 4.67 |
| Strouhal Number | $St$ | 0 | 0 | 4.4 x $10^{-4}$ | 3.3 x $10^{-4}$ |

Table 1. Scaling parameters; exp-experiment; num-numerical simulation; flt-spaceflight conditions

| | | **Phoenix REM:100% throttle** | | **MSL MLE:100% throttle** | |
|---|---|---|---|---|---|
| | | **½ scale** | **full-scale** | **¼ scale** | **full-scale** |
| Min area ($m^2$) | $A^*$ | 3.83 x $10^{-5}$ | 15.3 x $10^{-5}$ | 6.9 x $10^{-5}$ | 110.3 x $10^{-5}$ |
| Exit area ($m^2$) | $A_e$ | 0.00079 | 0.00318 | 0.00193 | 0.03089 |
| Expansion ratio | $A_e/A^*$ | 20.7 | 20.7 | 28.0 | 28.0 |
| Mass flow rate (kg/s) | $\dot{m}$ | 0.11 | 0.16 | 0.28 | 1.52 |
| Chamber temp. (K) | $T_c$ | 300 | 1114 | 300.0 | 1218.2 |
| Chamber press. (kPa) | $P_c$ | 1240 | 1240 | 1765 | 1765 |
| Exit density ($kg/m^3$) | $\rho_e$ | 0.194 | 0.026 | 0.202 | 0.023 |
| Exit pressure (Pa) | $P_e$ | 3091 | 3241 | 2837 | 2927 |
| Exit temperature (K) | $T_e$ | 54 | 217 | 47 | 202 |
| Exit Mach | $M_e$ | 4.8 | 4.7 | 5.1 | 5.1 |
| Exit velocity (m/s) | $v_e$ | 713 | 1929 | 721 | 2123 |
| Thrust (N) | $F$ | 80 | 321 | 206 | 3313 |
| Time (s) | $T$ | 0.75,1.5,3.0 | < 2.0 | 1 | ~ 6 |
| Pulse frequency (Hz) | $F$ | 10 | 10 | N/A | N/A |
| Pulse width (ms) | $PW$ | ~65 | 55 | N/A | N/A |
| Altitude (m) | $h/d$ | 8.4-25 | 8.4-80 | 34.5 | 34.5 – 50.0 |
| Slope (deg) | $\Phi$ | 0 | ~0 | 0.0, 22.5 | 0.0, 22.5 |
| Specific heat ratio | $\Gamma$ | 1.40 | 1.38 | 1.40 | 1.38 |

Table 2. Dimensional parameters.

## EXPERIMENTAL METHODOLOGY

JET-GROUND INTERACTIONS DUE TO THE SUBSCALE PHOENIX REM THRUSTER PLUMES

A half-scale cold flow (non-heated jet) test-bed (CFTB) was developed to study the impingement of supersonic pulsed jets on a flat surface at Mars ambient pressure. The thruster firing frequency, the duration of the pressure pulse, and the chamber pressure ($P_C$) were adjustable. Dry compressed nitrogen gas at room temperature was used to simulate hydrazine decomposition products because it has a similar specific heat capacity ratio. The importance of this parameter in scaling is discussed in the following section. Fast response absolute micro-electro-mechanical system (MEMS) pressure sensors were placed radially across the impingement plate at a spacing distance of 27.5 mm between sensors. A gauge pressure transducer was placed at the nozzle inlet which measured the stagnation pressure of the incoming flow. Both transducer and MEMS sensors each had a response time of 1 msec. One thermocouple was also placed at the plate's centerline. One ½ scale thruster with a similar nozzle contour profile as the Phoenix MR-107 descent engine nozzle was horizontally mounted inside a thermal-vacuum chamber, which was set to an ambient pressure of 690 Pa and ambient temperature of 290 K. The ambient pressure within the thermal-vacuum chamber was generated by a mechanical pump and monitored by a transducer with a response time of 1 msec at a maximum sensitivity of 1000 Pa. During the constant velocity descent phase of the Phoenix spacecraft, the rocket plumes are pulsed at a 10 Hz frequency, with a 55-45 msec pulse width, a maximum chamber pressure ($P_{C\text{-}max}$) of 1.24 MPa, and a chamber pressure ($P_C$) rate of change during engine startup/shutdown cycles of approximately 152 MPa/s. Our CFTB system generally met all these requirements as shown in Table 2, but it took many design iterations to obtain the required performance. The thruster chamber pressure and the ground impingement pressures ($P_s$) were measured at a sampling rate of 48 kHz. The thruster altitude (i.e., the distance of the thruster exit plane from the impingement plate) can be adjusted from 0.25 m (scaled touchdown altitude) to 1 m above the surface.

For the full-scale and subscale Phoenix REM nozzles, the jets were pulsed with similar initial conditions described in Table 2. Although during Phoenix descent, where twelve engines were firing, we used a single nozzle to validate the numerical solutions at University of Michigan. The plume interactions with the surface at a 0º slope for the Phoenix spacecraft lasted less than 2 s which decreased in altitude from ~60*d* to 8.4*d*, touchdown altitude[23]. The parameters that we varied were the jet expansion ratio and the altitude from 8.4*d* to 25*d*. A more detailed experimental setup for the subscale Phoenix cases is presented in Plemmons et al [2008][x].

JET-GROUND INTERACTIONS DUE TO THE SUBSCALE MSL MLE THRUSTER PLUMES

These experiments were conducted at NASA Ames Research Center in a 4000 $m^3$ vacuum test chamber at the Planetary Aeolian Laboratory (PAL) which is directed by Arizona State University. The vacuum chamber has a height of 30 m and a diameter of ~15 m and it can be evacuated to 350 Pa by a steam ejector driven vacuum system. The chamber was backfilled with air for all tests conducted. Its' average temperature was approximately 280 K with an average relative humidity of 5-10%. For our tests, we varied the atmospheric pressure within the vacuum chamber between 0.7 kPa and 101.3 kPa (± 1% of full-scale). Due to the steam ejectors and large chamber volume, atmospheric pressure and temperature were constant during the entire test duration.

Dry nitrogen flows from the 14 MPa high pressure supply cylinder which is controlled by a regulator to two reservoir tanks in parallel that are set to a specified total pressure dependent on the throttle levels to be simulated (Fig. 3). The total pressure in the reservoir tanks are set to ~1850 kPa for 100% MLE throttle setting. The other two settings used are 60% and 30% throttle. To minimize the loss of total pressure as a function of time, the regulator supplies the needed flow rate to prevent premature choking. We can remotely set the controls for operating the jet such as duration, pulse width, pulse frequency and total pressure within the nozzle chamber ($P_c$). The flow then passes through a solenoid valve, which is remotely activated, and into a converging-diverging nozzle. The solenoid valve and propellant system performance was tested to ensure a relatively constant $P_c$ that simulates the profiles from the MLE hot-fire tests. A schematic of the experimental setup is shown in Figure 3.

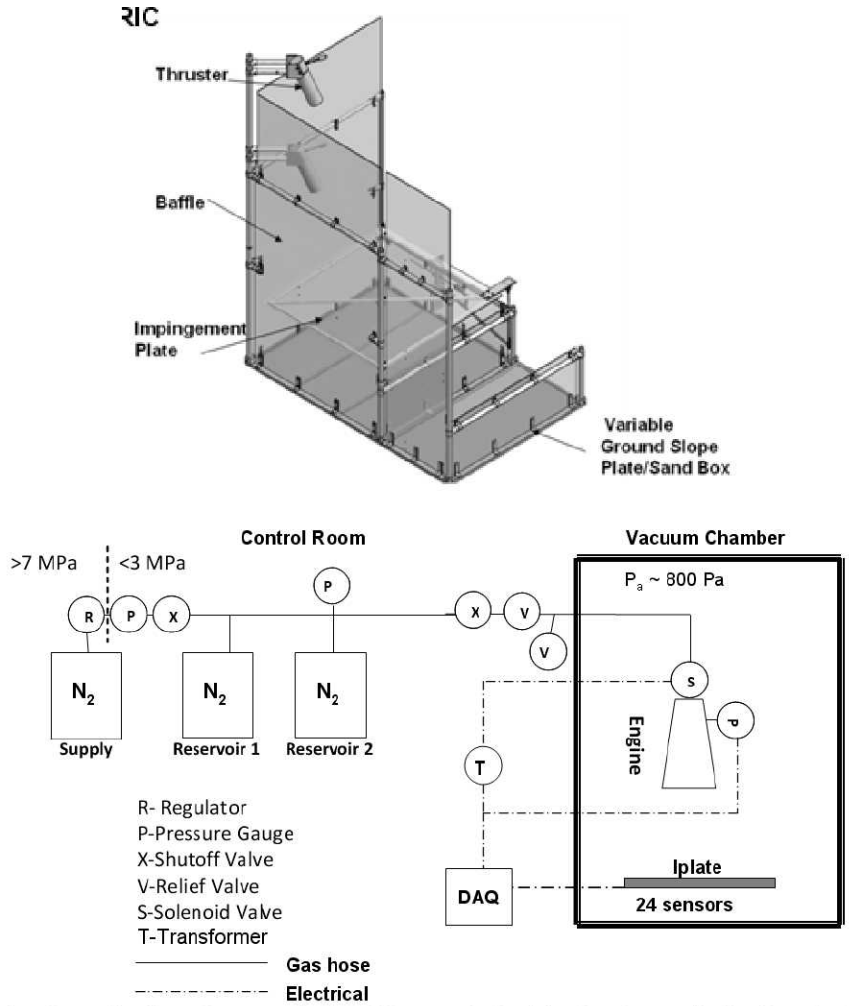


Figure 3. Isometric view (top) and general plumbing and electrical schematic (bottom) of MSL MLE plume impingement test setup at the NASA Ames Research Center.

A converging-diverging nozzle with an area ratio of 28 was used to match the nozzle contours on the main landing engines (MLE) of the Mars Science Laboratory (MSL) Descent Stage spacecraft[24]. The subscale nozzle was canted to 22.5° to accurately simulate the nozzle orientation and configuration on the MSL Descent Stage (Fig. 3). The experimental nozzle is ¼ scale of the MLE flight system with an exit Mach number of 5. The parameters that we varied are the nozzle pressure ratio (NPR) or the jet expansion ratio ($e$), and ground slope. The NPR ranged from 12 to 1200 and the jet expansion ratio spanned between 0.02 and 3.00. The MLE simulations are operated at an altitude of 35$d$ with ground slopes of 0° and 22.5°. The test matrix is included in Table 3. This simulates the lowest altitude the MSL descent stage approaches the surface prior to separation of the MSL rover[24]. Other important nozzle and test specifications, such as area ratio, exit diameter, etc are tabulated in Table 2. The exhausting jet impinges onto a 1.2 m x 1.8 m aluminum plate (iplate) of which 24 surficial fast responsive piezoresistive pressure sensors are located (Fig. 3). These sensors are then recorded at 1 kHz by a simultaneous sampling data acquisition system with an accuracy of ±0.1% of full-scale. These pressure sensors are scattered in high concentration near the expected impingement point, denoted as an "x", with lower concentration outward from this point. The ground pressure contour plots use linear interpolation between sensor data points. The stagnation pressure within the inlet nozzle chamber ($P_c$) is recorded by a fast responsive pressure transducer at 1 kHz with an accuracy of ±0.25% of full-scale.

| Test | Atmos.(Pa) | Ground (deg) | Height (m) | Throttle Level (%) |
|---|---|---|---|---|
| 1 | 800 | 0.0 | 1.73 | 60.00 |
| 2 | 733 | 0.0 | 1.73 | 60.00 |
| 3 | 933 | 0.0 | 1.73 | 100.00 |
| 4 | 1470 | 0.0 | 1.73 | 100.00 |
| 5 | 1530 | 22.5 | 1.73 | 96.67 |
| 6 | 1610 | 22.5 | 1.73 | 91.67 |
| 7 | 1730 | 22.5 | 1.73 | 86.67 |
| 8 | 1730 | 22.5 | 1.73 | 80.00 |
| 9 | 1800 | 22.5 | 1.73 | 73.33 |
| 10 | 1840 | 22.5 | 1.73 | 68.33 |
| 11 | 1870 | 22.5 | 1.73 | 63.16 |
| 12 | 1880 | 22.5 | 1.73 | 56.84 |
| 13 | 1930 | 22.5 | 1.73 | 53.68 |
| 14 | 2000 | 22.5 | 1.73 | 47.37 |
| 15 | 2000 | 22.5 | 1.73 | 44.21 |
| 16 | 2030 | 22.5 | 1.73 | 41.05 |
| 17 | 2070 | 22.5 | 1.73 | 37.89 |
| 18 | 2110 | 22.5 | 1.73 | 34.74 |
| 19 | 2470 | 1.9 | 1.73 | 31.58 |
| 20 | 2530 | 1.9 | 1.73 | 28.42 |
| 21 | 101325 | 22.5 | 1.73 | 100.00 |
| 22 | 101325 | 0.0 | 1.73 | 100.00 |

Table 3. Test Matrix

Two transparent baffle planes at 90° as seen in Figure 4 (Plexiglass) are used in our experiments to simulate the effects of the outboard thrusters shown in Figure 4 as done for the Phoenix-based experiments[25,26]. Only one MLE per quadrant is firing during descent. The jets from symmetrically opposing thrusters stagnate at the midline between the two engines. These planes were also used to minimize the complexity of the experiment.

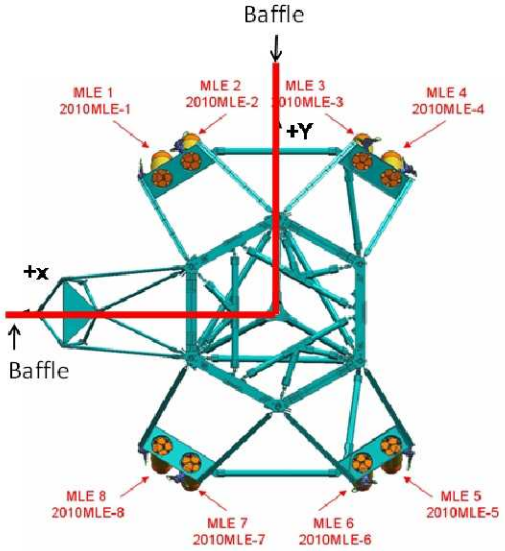


Figure 4.Top-down schematic of the Mars Science Laboratory Descent Stage with superimposed baffles to simulate outboard thrusters as implemented in experimental testbed. *Courtesy of NASA/JPL-Caltech*

## NUMERICAL METHODS

JET-GROUND INTERACTIONS DUE TO MSL MLE THRUSTER PLUMES

Computations were carried out using the OVERFLOW 2.1 code, a three-dimensional time-marching implicit code that uses structured overset grid systems[27]. The full Navier-Stokes equations were solved over the entire domain including the nozzle internal flow, where a total temperature, total pressure boundary condition was used to satisfy inlet conditions. Nozzle interior, nozzle enclosure, jet plume, and far-field domain grids of ~12 million cells were generated to encompass the experimental setup with viscous spacing at solid wall surfaces. A shear stress turbulence (SST) model with compressibility correction was used for all computations, as it has been shown to preserve jet plume velocity profiles better than other models available in the solver[28]. All simulations for full-scale and sub-scale studies were steady-state solutions.

JET-GROUND INTERACTIONS DUE TO PHOENIX REM THRUSTER PLUMES

Two flow solvers were used to obtain numerical solutions for both full-scale and subscale flow physics of the interaction of the underexpanded supersonic thruster plumes from the Phoenix REM nozzle with the flat surface. Transient and steady-state solutions were developed from these numerical solvers. Both 3-D and axisymmetric solutions were developed. The two numerical codes used were Aerosoft GASP[29] and ANSYS FLUENT [*ANSYS Inc.*, 2009]. GASP was used to model both full-scale and subscale cases.

Transient and steady state Reynolds averaged Navier-Stokes equations were solved by the GASP code, using both axisymmetric and 3-D density based solver. To resolve the shock waves, the Van Leer flux splitting scheme is used which is dissipative and leads to the smearing of shocks [*Van Leer et al.,* 1990][30]. The laminar model used for these cases. To obtain time accurate results, a dual implicit time stepping derived solution is selected. A single species frozen flow model is assumed. Total pressure and temperature are the inlet boundary conditions and the outlet is a Riemann subsonic inflow/outflow which takes into consideration the potential entrainment of exhaust near the nozzle. The pressure inlet boundary condition for the transient simulations was forced by using test data from both the hot-fire rocket motor tests and cold flow experimental tests. Grid independence is applied to both axisymmetric and 3-d meshes. Internal nozzle flow solution was calculated as well. For the 3-d models, a symmetry plane is developed between the pair of thrusters to obtain the solution for a 60° wedge of the spacecraft[26,31]. This was done because 180° and 60° wedges showed very similar flow fields and ground pressure results due to the development of stagnation planes formed by the exhaust plume interactions of the two pairs of descent thrusters[31]. This also decreased the complexity of the flow domain. Four million grid cells were generated for the fine mesh 3-D models.

Another numerical solver called ANSYS FLUENT was applied to further confirm the results of the experimental test data. The turbulence model used was the renormalization group (RNG) of $k$-$\varepsilon$[32] and to confirm that numerical dissipation did not significantly affect the shock wave profiles, an inviscid case was also run. Transient axisymmetric and 3-D solutions with a 1 μs dual implicit time stepping scheme with adaptive grid meshing was applied to resolve the shock waves in the flow domain. Pressure inlet and outlet were the applied boundary conditions. Convergence was observed for 2$^{nd}$ order upwind discretization schemes for all state parameters.

## RESULTS AND DISCUSSION

Spatial and temporal ground pressure profiles along with Mach contours are used to analyze the flow physics of supersonic impinging jets by mainly varying the jet expansion ratios and Strouhal numbers. Correlation of this data with temporal $P_c$ profiles and other initial conditions such as nozzle exit pressure, mass flow rate and thrust added insight into the physics. These values are tabulated in Table 2. All ground pressure values ($P_g$) are normalized by $P_c$ and physical dimensions are normalized by the nozzle exit diameter, $d$.

EXPERIMENTAL RESULTS DUE TO SUBSCALE MSL MLE THRUSTER PLUMES

For the temporal ground pressure profiles, we record the ground pressure rise and settling times, maximum and steady state pressure values, atmospheric pressure (vacuum chamber) and $P_c$ profiles. All these steady tests were performed for one second duration. We observe transient ground overpressures on the order of 100% to 30% increase from its' steady state values for $e > 2$ (Fig. 5, solid line). However, no repetitive ground shock frequencies were observed for these cases. These overpressures span from 0.1 s to ~0.3 s during the $P_c$ rise due to engine start-up as observed in Figure 5 (dashed line). There is a steady-state ground pressure regime that lasts from 0.3 s to ~1.0 s. After this point, there is a simultaneous rapid ground pressure decline with a sudden decrease in the $P_c$ due to engine shut-down. For $e < 2$, there are no characteristic overpressure and exhibits relatively steady and much smaller pressure amplitudes as seen from Figure 5A,B. At $e = 0.02$ (Earth atmospheric pressure), the ground pressure maximum is well below 0.001.

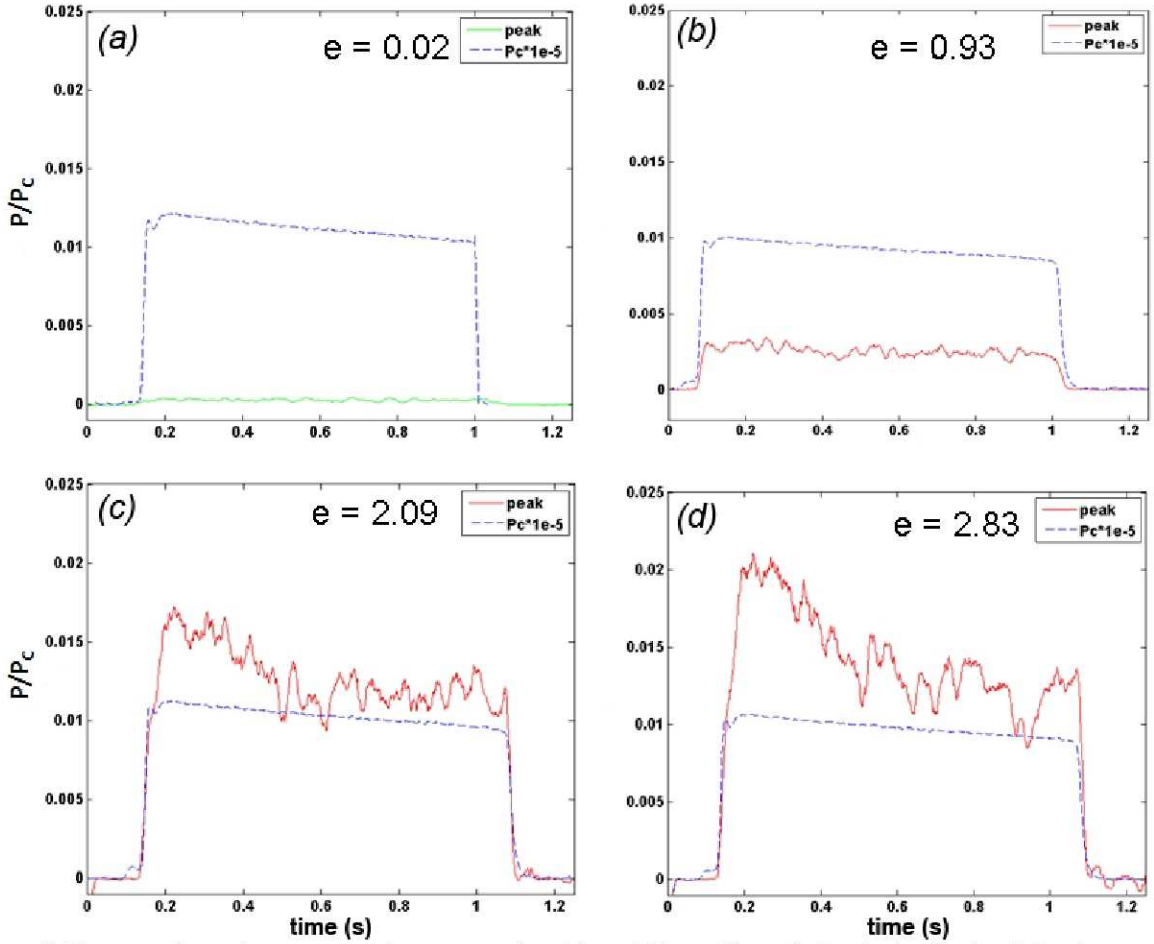


Figure 5. Temporal maximum ground pressure (peak) and $P_C$ profiles of steady impinging jets at an altitude of ~35*d* for varying jet expansion ratios of Test 22 (A), Test 11 (B), Test 1 (C) and Test 2 (D). See Movie D7 and D8 for Test 2 and Test 22, respectively.

For the spatial ground pressure profiles, we developed ground pressure contour maps at the maximum overpressure value at $t = 0.25$ s (Fig. 6) and steady-state values at $t = 0.45$ s. From these contour maps, we observe that at $e = 2.09$ and $e = 2.83$, there is a radial pressure footprint which is bounded by the sensors and it is ~2*d* in diameter (Fig. 6 C,D). There is a large normalized pressure gradient, $\nabla$, (Eqn. 26) of 0.017 at $e = 2.83$ determined from the periphery of the footprint. For $e = 0.02$, we do not observe these large pressure gradients $(\nabla < 0.001)$ and there is a modest increase in pressure that spans a distance of ~7*d* as seen in Figure 6A. For $e = 0.93$ and less, the pressure gradient is much smaller in magnitude $(\nabla < 0.0025)$ and more gradual, typical of a Gaussian distribution. The normalized pressure gradient is defined as follows:

$$\nabla = \frac{\Delta P_g}{P_C} \frac{d}{\Delta x} \qquad (26)$$

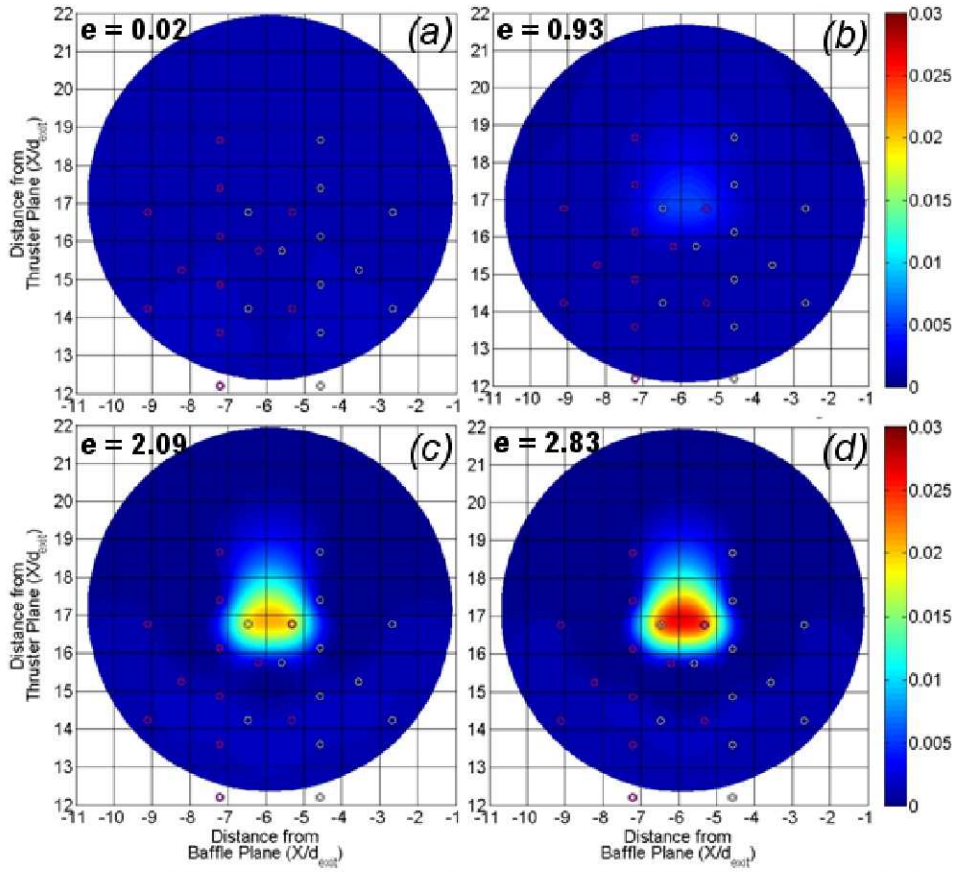


Figure 6. Ground spatial pressure profiles of steady impinging jets at an altitude of 35*d* for varying jet expansion ratios for test cases presented in Fig. 5. The colorbar depicts the normalized ground pressure values.

Figure 7 shows how the jet expansion ratio affects normalized impingement pressure ($P_g/P_c$) from our experiments. We observe for our tests that there is a maximum for overpressure ($P_g/P_c$ = 0.005) and steady ground pressure ($P_g/P_c$ = 0.015) values for $e$ > 2. The overpressure is defined as the difference between maximum and steady-state ground pressure values. This is an increase by a factor of 5 compared to amplitudes at $e$ < 2. These amplitudes are relatively constant between $e$ = 2 to $e$ = 0.25 with a slight increase in the steady ground pressure magnitude ($P_g/P_c$). We notice a minimum in steady and overpressures at $e$ = 0.02.

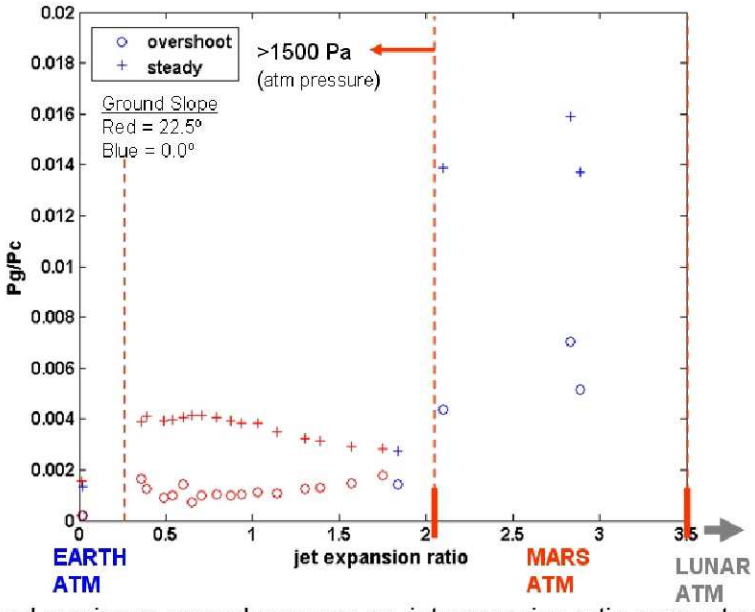


Figure 7. Normalized maximum ground pressure vs. jet expansion ratio curve at an altitude of ~35*d*.

Normalized ground pressure rise rates are how quickly the normalized ground pressure values rise to the maximum amplitude due to engine start-up. Figure 8 shows the rise rates (1/s) as a function of the jet expansion ratio. We observe a linear increase in the pressure rise rate with increasing jet expansion ratio for $e > 0.5$. We observe the largest rise rates for $e > 2$ with an increase by a factor of ~4 from the values compared to $e < 1.5$. The normalized settling rates, which determine how quickly the ground overpressure values settle to its' steady-state values, do not show a characteristic trend with respect to the jet expansion ratio.

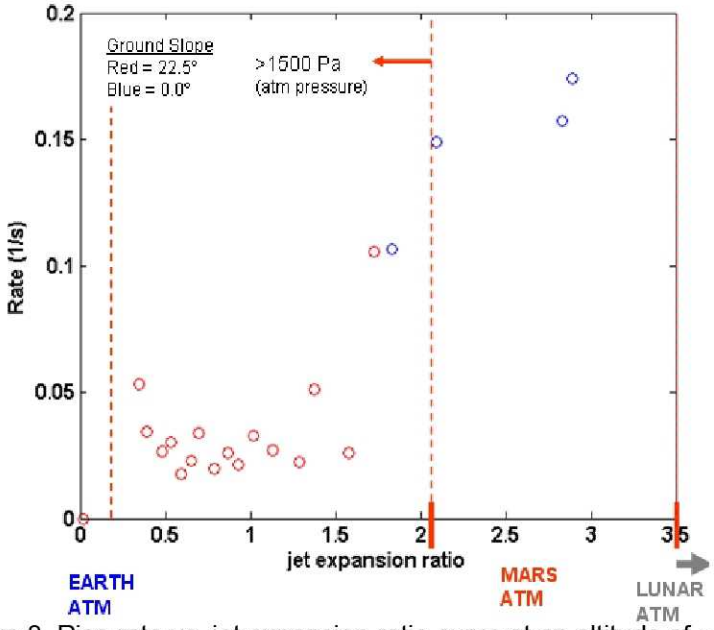


Figure 8. Rise rate vs. jet expansion ratio curve at an altitude of ~35*d*.

EXPERIMENTAL RESULTS DUE TO PHOENIX REM THRUSTER PLUMES

For experimental results in understanding pulsed jet effects on ground pressure (non-zero Strouhal numbers), we used two different jet expansion ratios: $e$ ~4.5 – 3.8 (moderately underexpanded) and $e$ = 0.02 (highly over-expanded) at an altitude of 8.4$d$. The most interesting feature in the temporal pressure profiles analysis at $e$ = 4.4 are the transient overpressures observed during engine start-up and shut-down phases[x]. These peaks demonstrated normalized rise rates on the order of 6.0. These overpressures were repeatable and did not demonstrate hysteresis.

The spatial ground pressure profile for $e$ = 4.4 were also radial with a pressure footprint diameter of ~3.2$d$. As noted for the MSL experimental measurements, for highly over-expanded jets, the pressure footprint was more diffuse with a smaller magnitude and a Gaussian distribution and did not indicate large pressure gradients as observed for moderately under-expanded jets. The spatial pressure profile for moderately underexpanded jets is non-Gaussian and there are minor pressure peaks observed at ± 1.6$d$ due to the effects of oblique tail shocks.

NUMERICAL RESULTS DUE TO MSL MLE THRUSTER PLUMES

Numerical results are first used to compare subscale ground pressure spatial and temporal profiles and near-field plume structure with measured quantities. Once in similar agreement, Mach contours can be used in conjunction with ground pressure profiles to understand the flow physics. This approach was used to obtain an understanding of our observations.

The Mach contours for the MLE plumes have a maximum Mach number of ~10 with a shock cell length of 14$d$. Approximately 2.5 shock cells are formed within the plume. As can be seen from Figure 9, the plumes are highly collimated even to distances greater than 35$d$. This is a very important characteristic that will be discussed in a later section. We observe characteristic flow features such as a plate shock with a diameter of ~2$d$ and wall jet as observed by Lamont and Hunt [1968][1]. Due to an oblique jet interaction, the wall jet predominantly propagates in a +x direction as shown in Figure 9.

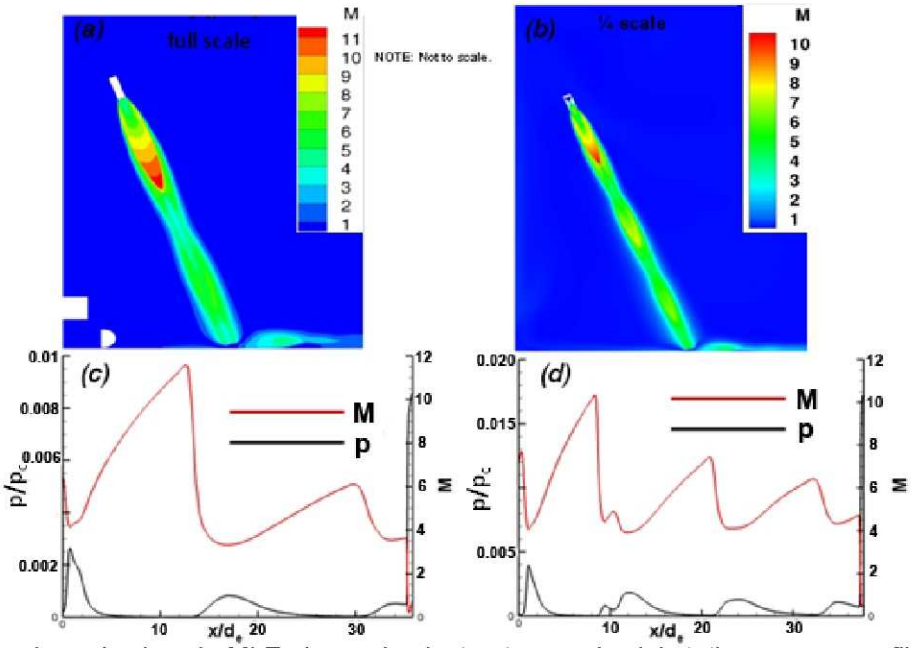


Figure 9. Full-scale and subscale MLE plume shock structure and axial static pressure profiles. *(a,b)*, Full-scale and subscale numerical solutions of the Mach contour at an altitude of ~35$d$ for MLE plumes at 100% throttle; *(c,d)*, Full-scale and subscale numerical solutions of Mach (red line) and static pressure (black line) profiles as a function of $x/d_e$ (axial distance along the plume).

All solutions were for steady-state conditions and hence only steady ground spatial pressure profiles are recorded (Fig. 10). This exhibits a radial pressure footprint with high pressure gradients of

0.026 and a diameter of 1.75*d*. There is an asymmetry in the profile and the highest pressure regions reach a nondimensional value of 0.028, which is approximately 0.5*d* from the plume centerline. The average ground pressure value within the footprint area is within the range of 0.018.

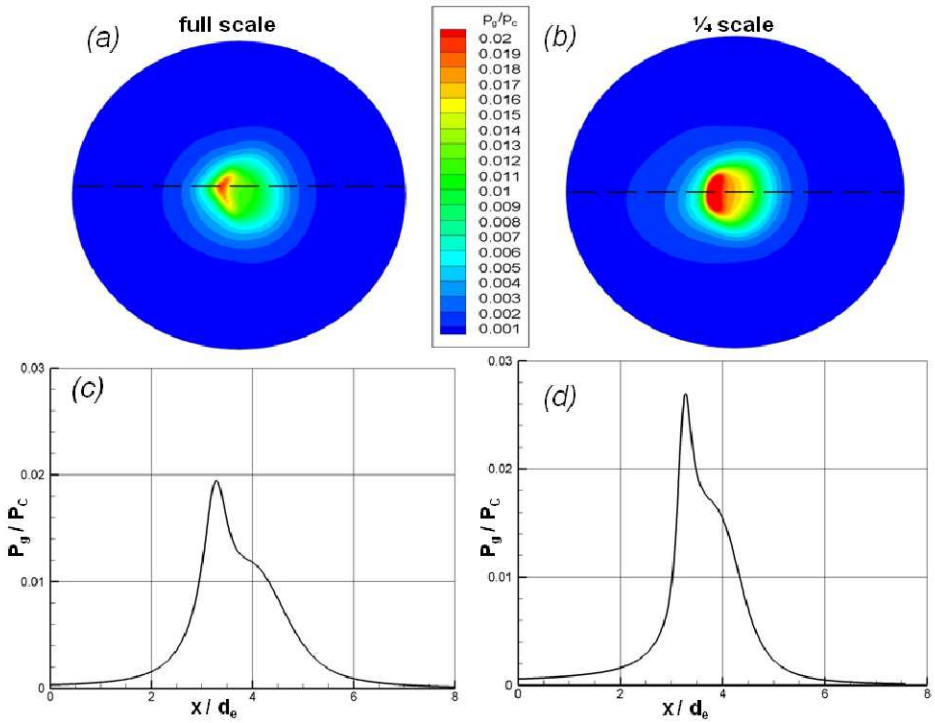


Figure 10. Numerical solutions between *(b,d)* subscale and *(a,c)* full-scale spatial ground pressure profiles of MLE plume interactions at 35*d* at 100% throttle. Subscale and full-scale numerical solutions of normalized ground pressure profiles ($P_g/P_c$) as a function of $x/d_e$ along the dotted lines shown in the a and b panels.

From Figure 11, we observe good agreement (within ±7.5%) between numerical solutions and experimental measurements for normalized spatial ground pressure profiles at *e* ~3. The pressure footprint diameter, normalized maximum ground pressure values and pressure gradients are similar for both simulation and measurements. The numerical solution show a slightly smaller pressure footprint (see Results section). There are some minor discrepancies in the features such as the lack of capturing the high pressure asymmetry region which is due to lower measurement resolution than the numerical simulation and sensitivity in turbulence modeling.

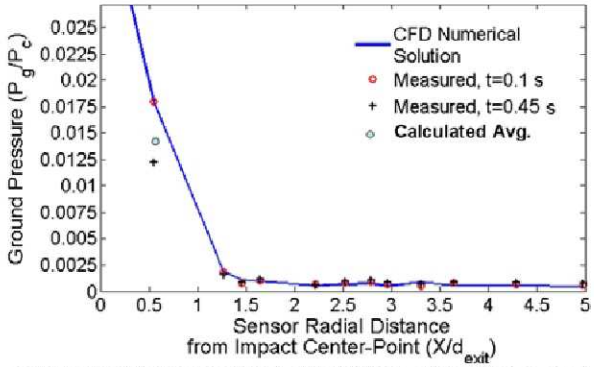


Figure 11. Numerical solution compared to measured quantities at $t$ = 0.1 s and $t$ = 0.45 s for steady underexpanded $N_2$ jet impingement at *e* ~3 at an altitude of 35*d* (Test 3).

NUMERICAL AND EXPERIMENTAL RESULTS DUE TO PHOENIX REM THRUSTER PLUMES

Transient and steady state solutions were developed for the pulsed supersonic jets impinging at the surface at various altitudes. Simulations at two altitudes are presented here: 8.4*d* and 25*d*. Numerical simulations show that an underexpanded supersonic jet with an *e* = 4.4 at an altitude of 25*d* results in the development of a normal plate shock with a diameter of ~2*d* and wall jets that propagate in the ±x direction (Fig. 13). Two shock cells are observed with a length of ~12*d* within the plume structure at an altitude of 25*d*. Here, once again, the plume structure is collimated as observed for the MLE thruster plume numerical simulations.

According to Figure 12A,B, the numerical simulations and experimental measurements at an altitude of 8.4*d* show good agreement (within an average of +/-10%) in both temporal and spatial ground pressure profiles at the far-field and near-field regimes for underexpanded jet at *e* ~4.4. They both show ground overpressures at a 20 Hz frequency and similar quasi-steady ground pressure magnitude, footprint area and pressure gradients. We also observe good agreement between numerical simulation and shadowgraph imaging in the plume shock structure at the near-field regime (Fig.12 b,c). The numerical simulation exhibits a plume expansion angle from the nozzle exit plane of approximately 25º. This also shows good agreement with the findings from Clark et al., [1971][10]. This value is somewhat less for our shadowgraph images which show an expansion angle of 22º.

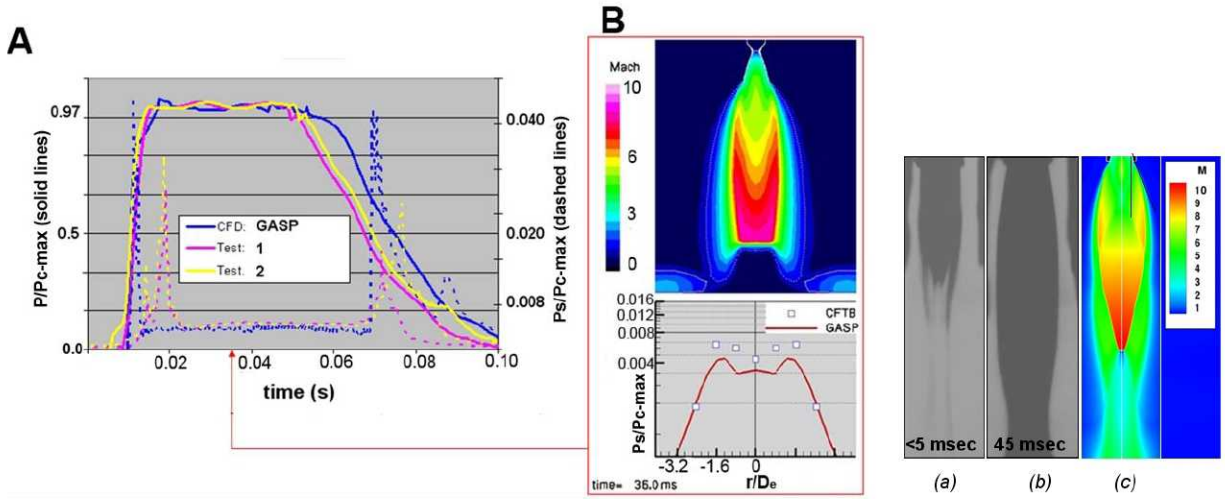


Figure 12. Comparison of axisymmetric numerical simulations and experimental measurements of pulsed supersonic $N_2$ jet interactions at $h/D_e$ = 8.4. (A) Temporal centerline ground pressure (dashed lines) and $P_c$ (solid line) profiles; (B) Spatial ground pressure profiles and Mach contour. [*Gulick*, 2006] *(a)* Shadowgraph image of a near-field underexpanded jet (*e* ~4.4) at < 5 ms during engine start-up and *(b)* during full-throttle and *(c)* numerical solution during full-throttle

JET EXPANSION RATIO

The jet expansion ratio is one of the most important factors in determining ground pressure profiles at high altitudes (*h* > 5*d*). The jet expansion ratio influences the near-field and far-field plume structure. For *e* > 1 (underexpanded jets), the expansion fans form at the lip of the nozzle, causing the plume to expand outward with respect to the normal increasing the plume expansion angle ($\theta$ > 0º). For *e* < 1 (overexpanded jets) leads to reflected oblique shock waves that cause a decrease in the plume expansion angle with respect to the normal ($\theta$ < 0º). For *e* = 1 (perfectly expanded), this prevents the formation of expansion and shock waves and the plume expansion angle is zero. As a result of the low planetary atmospheric pressure on Mars and the moon, most of the thruster jets observed during spacecraft landings on these celestial bodies is underexpanded.

From Figure 7, it can be seen that the normalized ground pressure value increases by a factor of five for jet expansion ratio greater than 2. It can also be seen that for very low *e* on the order of 0.02 the ground pressure was minimal. Numerical simulations that were validated by experimental tests show in

Figure 13 that the Mach contours and plume structure are also considerably different between *e* ~4.5 and *e* = 0.02. For moderately underexpanded jets (*e* ~4.5), the plume structure has compressed and collimated shock cells that are formed until a downstream distance is reached when plume and ambient static pressure are in equilibrium. This downstream distance, supersonic core length (*x*), is considerably larger for moderately underexpanded jets as compared to highly over-expanded jets (*e* ~0.02) as shown in Figure 13. This classification of jets may develop a stable plate shock at the surface and a propagating wall jet.

The relatively larger ambient pressure for highly over-expanded jets (*e* << 1) leads to the formation of reflected oblique and normal shock waves which may occur at the diverging section of the nozzle. Boundary-layer separation at the diverging section can lead to attenuation of the jet[33]. Once a strong normal shock wave forms at the diverging section (Fig. 13), this results in the propagation of weak shock waves which leads to flow separation and shock wave instability. The shock wave is further attenuated by the interaction and mixing of the shock with the dense shear layer at the jet boundary which leads to Kelvin-Helmholtz instabilities. Due to overexpansion, the atmospheric free surface boundary pinches the jet inward, leading to an axial increase in the turbulent mixing layer. This decreases *x* and results in the rapid decay of the plume structure to a fully turbulent subsonic jet with a linear spreading profile[29]. As a result of the spreading profile, large altitudes and subsonic flow field, normal plate shocks are not developed above the surface. This prevents the formation of large pressure gradients at the surface as well as the formation of supersonic wall jets.

For *e* >> 1, highly underexpanded jets shown in Figure 13, we also observe a decrease in normalized ground pressure profiles and this is due to a large plume expansion angle. The shock propagation of a large expansion plume results in a large areal plate shock as observed by Clark et al. [1971][10] which significantly reduces the normalized ground pressure since pressure is inversely dependent on area. Another mechanism may be due to the increased pressure losses due to a normal shock wave or a Mach disk formed within the near-field regime at high *e* as opposed to the unsteady oblique shock waves developed in the far-field regime at lower jet expansion ratios.

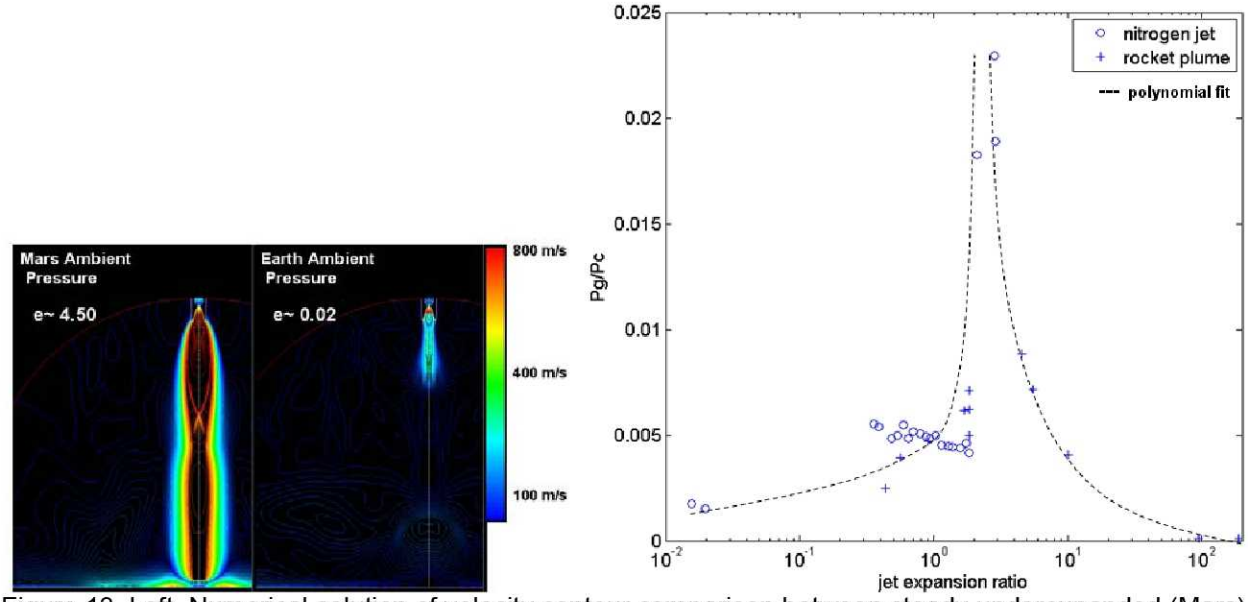


Figure 13. Left, Numerical solution of velocity contour comparison between steady underexpanded (Mars) and highly overexpanded (Earth) supersonic jets at an altitude of 25*d*. Right, Normalized centerline ground pressure vs. jet expansion ratio for nitrogen jets and rocket plumes at an altitude of ~35*d*.

We presented data above of the comparison of supersonic nitrogen jets and rocket plumes from monopropellant and bi-propellant rocket motors at an altitude of ~35*d* (Fig. 13). All nitrogen jets and rocket plumes demonstrate an exit Mach number of ~5[10,25,34]. The monopropellant rocket motors use hydrazine as the fuel which combusts at a $T_C$ of greater than 1000 K, releasing $N_2$, $H_2$ and $NH_3$ as low

density exhaust species. The bi-propellant uses methyl hydrazine as the fuel and nitric oxides as the oxidizer[34]. We show good agreement (within ±12.5%) in the trend between nitrogen jets and rocket plumes in which the highest normalized ground pressure values have jet expansion ratios between 2 and 5 as observed in our studies (Fig. 13). Rocket plumes also exhibit minimal normalized ground pressure values for highly over-expanded ($e$ < 0.5) and underexpanded jets ($e$ >> 5). Hence, to obtain accurate risk assessment of spacecraft landings on Mars and the moon without changing the thrust conditions, it is critical to study these interactions at the appropriate atmospheric environments so that the jet expansion ratio is accurately simulated.

This analysis of jet expansion ratio is quite important to consider, because these values are dependent on the propulsion system and atmospheric density of the planets for our application. We can decrease the effects of thruster plumes on the surface by changing the propulsion system requirements or by landing at a different latitude and longitude on planets. For example, the atmospheric pressure on Mars can change from ~350 Pa to 1000 Pa depending on the location and time of day.

## SUPERSONIC CORE LENGTH

Supersonic core length can be inferred from ground pressure profiles. An indirect approach in measuring the supersonic core length is by varying the distance from a flat surface and monitoring the ground pressure. Supersonic core that propagates to the flat surface results in the formation of a plate shock which leads to steep pressure gradients as observed in Figure 6. We conclude from the previous section that there are large differences in the supersonic core length and spatial ground pressure profiles for highly overexpanded and moderately underexpanded jets at an altitude of 35$d$. In contrast to moderately underexpanded jets, we observe a very diffuse and Gaussian pressure profile for highly overexpanded jets ($e$ = 0.02) as depicted in Figure 6 and this leads to rapid decay of the plume structure which demonstrates a core length of less than ~5$d$ as shown in Figure 13. The experiments indicate that the supersonic core length developed by MLE plumes ($e$ ~3) propagate to at least a distance of 37$d$. This is also supported by Mach contours generated by the numerical simulations (Fig. 9). Numerical solutions show that REM plumes ($e$ ~4.4) have a supersonic core length of at least 25$d$ (Fig. 14). This is further supported by Inman et al. [2009][13] which shows with Planar Laser-Induced Fluorescence (PLIF) imaging that a collimated moderately underexpanded ($e$ = 5.4) turbulent nitrogen jet at Mach 2.6 has a supersonic core length to a distance of 31$d$. Scroggs and Settles [1968][8] show with Schlieren imaging that the supersonic core length increases with jet expansion ratio and Mach number. They recorded supersonic core lengths on the order of 35$d$ for $e$ = 4 and a Mach number of 2.2.

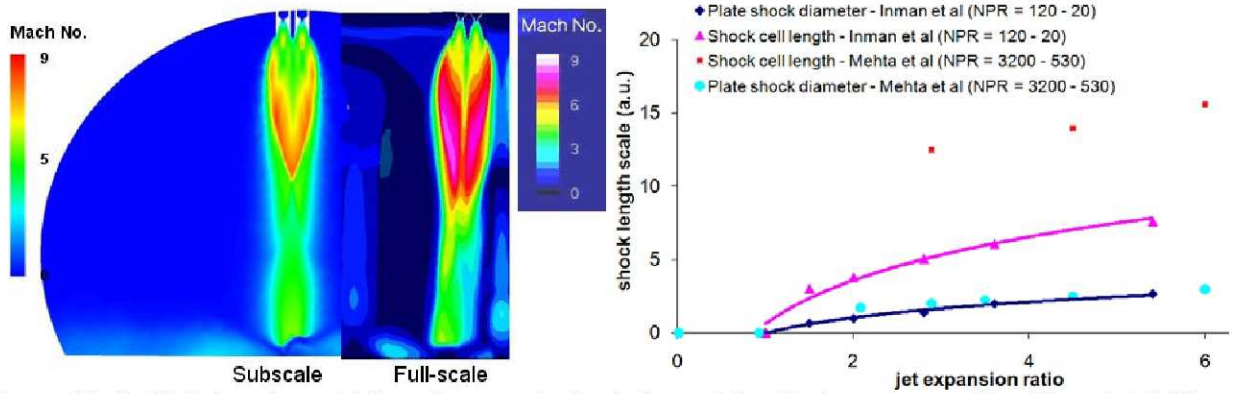


Figure 14. (Left) Subscale and full-scale numerical solutions of the Mach contours of the Phoenix REM plumes at an altitude of 25$d$.[31]; (Right) Normalized plate shock diameter and shock cell length as a function of the jet expansion ratio at an altitude of ~35$d$.

We determine the length of the shock cell, $x_s$, as a function of the jet expansion ratio. We see an increase in the shock cell length at higher NPR than at lower corresponding values[10]. The shock cell length increases logarithmically with increasing jet expansion ratio and increases linearly with nozzle exit diameter. Shock cell length may have a weak dependence on $M_e$.

PLATE SHOCK DYNAMICS

Plate shock dynamics lead to large ground pressure fluctuations and gradients at the surface. Figure 15 shows a numerical solution for the formation of a plate shock at the surface from a Mach 4.7 underexpanded jet ($e$ ~4.4). Prior to initial jet impact, shock waves accelerate toward the surface which initiates coalescing of the plume density and gas compression. After jet impingement, an unstable normal shock wave, plate shock, is formed above the surface and a transient high plume density is observed below the plate shock. This concentrated and localized plume density at high velocity results in larger ground pressures relative to subsonic flow fields. Hence, the large differences in ground pressure observed with varying jet expansion ratios. Overpressure due to plate shock formation is observed for both steady (MLE) and pulsed (REM) exhaust plumes. Overpressure occurs when the shock wave first impinges on the surface and the overpressure settles to quasi steady-state value upon stable formation of the plate shock. The non-Gaussian and high pressure gradients are characteristic of plate shock formation and the footprint is similar to the shock diameter.

There are some major differences in the shock dynamics between pulsed and steady (MSL) descent jets. The initial overpressure peak due to the MLE plumes are smaller than observed for the Phoenix cases and virtually absent during the engine shut-down phase and this may be due to the development of a much weaker normal shock at the surface. This could be attributed to a larger axial distance the shockwaves need to travel and the slope of the inclined surface. This could also be attributed to slower stagnation pressure rise and fall rates. Large instabilities in the plate shock may delay the formation of a fully-developed shock. Most importantly, the characteristic ground shock frequency observed for pulsed jets was entirely absent in these steady jet cases. This is mainly the result of engine cycling. However, during plate shock formation and collapse, high instability due to axial plate shock oscillations occur. This instability is further supported by the highly variable settling trend for $e$ > 1.5. Plate shock formation is also a function of the jet expansion ratio and altitude.

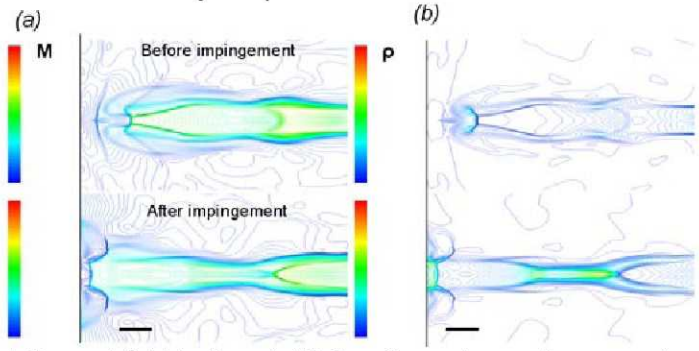


Figure 15. Numerical solutions of *(a)* Mach and *(b)* density contours of a pre and post normal shock wave interaction. Black bar depicts the length of the nozzle exit diameter.

From observations, a stable plate shock may not form for supersonic jets at $e$ below 1.75 at altitudes of 35$d$ and greater. As we approach a jet expansion ratio of one, shock cells within the plume disappear and lead to greater shock wave and static pressure attenuation at these large distances. This is also supported by Inman et al. [2009] which also shows a significant drop in the ground pressure at jet expansion ratios near and below unity.

A significant decrease in normalized ground pressure magnitude for $e$ < 2 may be attributed to the plate shock within the expansion regime of the shock cell. Large pressure fluctuations occur depending on whether the plate shock is within the expansion or compression regimes of the shock cell[x]. This is unlikely the result of our study due to the fact that successive points with decreasing jet expansion ratios ranging from $e$ = 1.90 to $e$ = 0.30 (changing shock structure profiles) lead to relatively constant normalized ground pressure magnitudes. Hence, the significant decrease in ground pressure (Figs. 7 and 13) is mainly due to the inability for a plate shock to develop at these expansion ratios and large downstream distances.

From Figure 14, the plate shock diameter is independent of both NPR and $M_e$, but shows logarithmic dependence on the jet expansion ratio and linear dependence on the nozzle exit diameter. These length scales profiles were determined by both numerical and experimental observations.

## COMPARISONS BETWEEN SUBSCALE AND FULL-SCALE TESTS

To ensure similar plume structure and ground pressure profiles between our subscale tests and exhaust plumes from both MSL and Phoenix rocket motors, scaling parameters derived above were used. There parameters govern the flow regime, specific plume energy density, compressibility and unsteady effects and the jet expansion ratio. Our goal is to determine whether these theoretical scaling parameters accurately determine the plume flow dynamics between cold gas jets and rocket plumes. These parameters are approximately similar between subscale and full-scale cases for both test programs (Table 1): Phoenix REM and MSL MLE. Experimental measurements and numerical solutions show that the Mach number, shock structure and spatial and temporal pressure profiles are in good agreement (within ±12.5%) between cold flow subscale and full-scale systems, Phoenix rocket exhaust plumes, at altitudes of 25*d* and 8.4*d*. This is observed for both single and dual thruster systems. For example, Figure 16 shows a numerical solution of a full-scale temporal and spatial ground pressure profiles for a full-scale rocket plume interaction from a single Phoenix descent engine (note the similarity in Fig. 12). The numerical solutions of the Mach contours between the subscale and full-scale MLE plumes show relatively good agreement (within ±12.5%) in both magnitude and shock structure (Fig. 9). The numerical solutions and experimental observations of the spatial ground pressure profiles between the MLE subscale and full-scale cases also show relatively good agreement (within ±12.5%) in pressure footprint area, normalized magnitude, asymmetry and pressure gradients (Fig. 10).

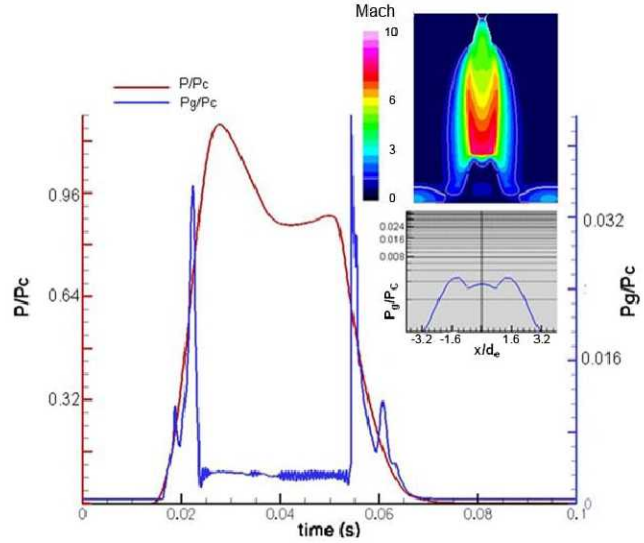


Figure 16. Full-scale (singe Phoenix REM plume interaction) numerical results of the spatial ($t$ = 0.036 s) and temporal normalized ground pressure profiles at an altitude of 8.4*d* at Mars atmospheric environment. [*Gulick*, 2006][31]

Numerical simulations were used to characterize the effects of rocket plumes on the ground at various altitudes. There are no large discrepancies observed for the numerical solutions of the Phoenix test cases, but the MSL test cases did show some minor differences. The ground pressure magnitude for the MSL cold gas jets is greater than the rocket plumes by a factor of 0.25. The plumes at subscale conditions are more compacted and collimated than for the full-scale case. The subscale jets also exhibit more frequent and shorter shock cells within the collimated plume. This is most likely attributed to a difference in the jet expansion ratio (Table 1).

Subscale experimental spatial and temporal ground pressure measurements show relatively good agreement with the full-scale numerical solutions for rocket plume impingement. The Phoenix and MSL test cases show few discrepancies, but overall show similar pressure footprint area, normalized

magnitude and pressure gradients. Due to limited pressure sensors and a decrease in resolution, we were not able to capture the asymmetry. Due to limitations in obtaining low vacuum in the chamber, we were not able to achieve exactly the same jet expansion ratio for the MLE cases as seen for the full-scale numerical simulations (Table 1). As a result of this extensive study, these scaling parameters applied to cold gas jets are critical in properly simulating rocket plume impingement effects. Further controlled experimental studies between full-scale rocket motors and supersonic cold gas jets are needed to confirm these results.

First, full-scale descent engines were numerically modeled and we observed good agreement with data from subscale experiments. This was an important result, because it partially confirmed the validity of our theoretical scaling laws. Full-scale rocket test firing at simulated martian conditions that record both temporal and spatial ground pressures are needed to fully validate these laws.

Once numerical and experimental results showed relatively good temporal and spatial agreement, the numerical code GASP was used to model full-scale three-dimensional cases for adjacent thruster plumes impinging at the surface. The computational domain spans a 60° wedge where two engines are modeled and is bounded by symmetry planes[31]. This domain is then extrapolated to obtain the Mach and pressure contour profile of the full 360° Phoenix Lander as shown in Figure 17. Due to adjacent plume interactions and non-linear shock/shock interactions as described in the previous section, the plate shock demonstrates noncoplanarity and oscillates in three-axes, leading to both asymmetric high pressure regions (Fig. 17A) and ground pressure fluctuations (Fig. 17B) during the quasi-steady regime. Most importantly, characteristic overpressure peaks are observed during rapid engine start-up and shut down, suggesting the mechanism of plate shock formation and collapse. These numerical simulations show that the spatial ground pressure profiles between the full-scale (Fig. 17) and subscale (Fig. 12) systems show good agreement in trends and further confirm the use of these scaling laws.

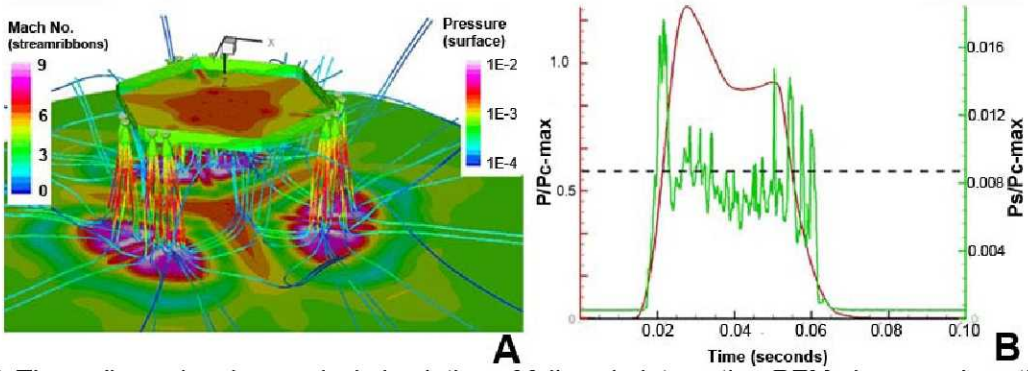


Figure 17. Three-dimensional numerical simulation of full-scale interacting REM plumes exhausting into a martian atmosphere. (A) Mach and normalized pressure contours of steady REM plumes interacting at the surface at an altitude of $h/D_e$ = 8.4 and 0° slope[31] (B) Centerline ground pressure (green curve) and $P_c$ (red curve) temporal profiles due to 0.1 s jet pulse at an altitude of $h/D_e$ = 21.9 and 0° slope. The dashed line is the centerline ground pressure solution for steady-state numerical simulation[31]

ASYMMETRIES DUE TO ADJACENT PLUME INTERACTIONS

Although most of the studies presented thus far are primarily concerned with single jet interactions, we will briefly discuss the ground pressure and shear stress (tau) behavior due to two adjacent underexpanded $N_2$ jets with a nozzle spacing of $x/D_e$ = 0.1, similar in geometric configuration as adjacent Phoenix descent engines. A 3-D steady state numerical simulation was developed to understand possible asymmetries at the surface. In contrast to the radial symmetry of single subsonic and supersonic jet interactions[x], adjacent jets develop large asymmetries in both ground pressure and wall shear stress parameters as shown in Figure 18. There are no symmetric ring-like contour profiles, but rather asymmetric semi-circular high pressure and shear stress regions. This may be attributed to shock-shock Riemann interactions[35] which develop a merged shock with higher strength at both the near-field and far-field regimes. Hence, the plate shock is almost twice in diameter as observed for a single jet case. This

merging could lead to a noncoplanar development of the normal shock, resulting in asymmetry in ground pressure. This may also affect both the tail shock and the flow behavior of the supersonic wall jets, leading to asymmetry in the wall shear stress. These wall jets are caused by flow expansion, developing mainly from flow across the tail shock and propagating along the surface (Figure 18). Hence, these results demonstrated the need for 3-D numerical simulations of the six pairs of Phoenix REM plume interacting at the surface.

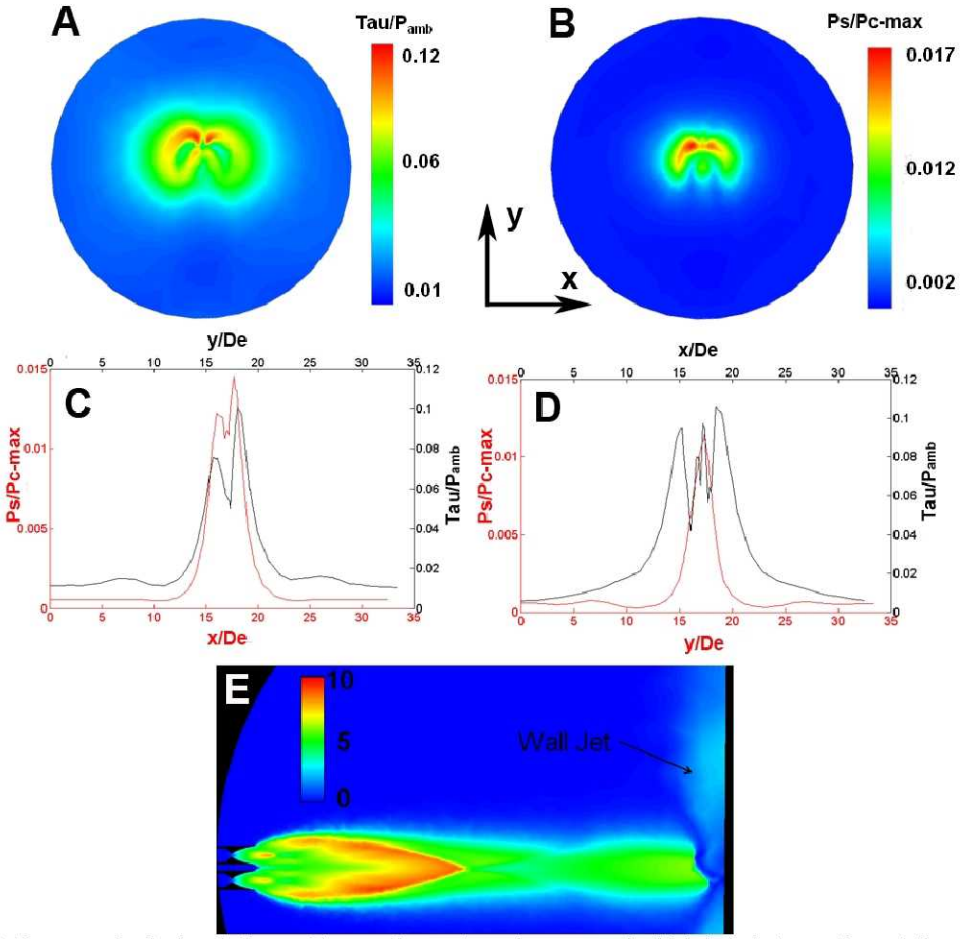


Figure 18 3-D numerical simulation of two adjacent underexpanded $N_2$ jets interacting at the surface at $h/D_e$ = 25. Contour s of (A) wall shear stress normalized by ambient pressure and (B) normalized ground pressure; (C,D) Tau and ground pressure profiles along the *x* and *y* centerlines. (E) Mach contour

## SITE-ALTERATION AND DUST LIFTING

Various mechanisms due to the rocket plume interactions can lead to significant soil erosion and dust lifting. The overpressures described above and the high surface shear stress associated with the supersonic wall jets can lead to soil erosion and dust lifting. Large and rapid pressure fluctuations might cause soil liquefaction[36]. Soil liquefaction is defined as the fluid-like state of granular media. Ground shock vibrations caused by these large transient overpressures super-imposed by the pulsing quasi-steady state overpressure regions may disrupt the soil and break the particle-to-particle cohesive forces. This can decrease the bearing capacity, maximum average contact pressure between the foundation and the soil to prevent shear failure, and increase the fluidization of the soil, possibly leading to lateral ground failure and crater formation[36]. The extent of ground failure depends on the soil properties, surface impingement temporal and spatial pressure profiles, ground shear stress[36] and the dynamic interactions between the thruster plume and the ground. The minimum ground pressure threshold before erosion

takes place at a simulated martian environment is approximately ~2 kPa for soil similar to dune sand or lunar nominal[25].

Also, depending on whether the shock cell is within the compression or expansion zone near the surface results in a non-linear behavior of ground pressure with altitude, which presents itself differently than for the asymptotic profiles of subsonic jets [37]. These pressures are relatively independent of altitude and oscillate around a mean value for small $h/D_e$ (< 40). The overpressure and quasi-steady state ground pressure can significantly change in magnitude as can be seen for the two non-dimensional altitude cases presented here: $h/D_e$ = 8.4 and 25. This high variability is further shown in Figure 19. We see good qualitative agreement between experimental observations of cold gas simulations[x] and 3-D numerical results of full-scale systems[32]. This variability may also lead to further disturbance of soil during spacecraft descent.

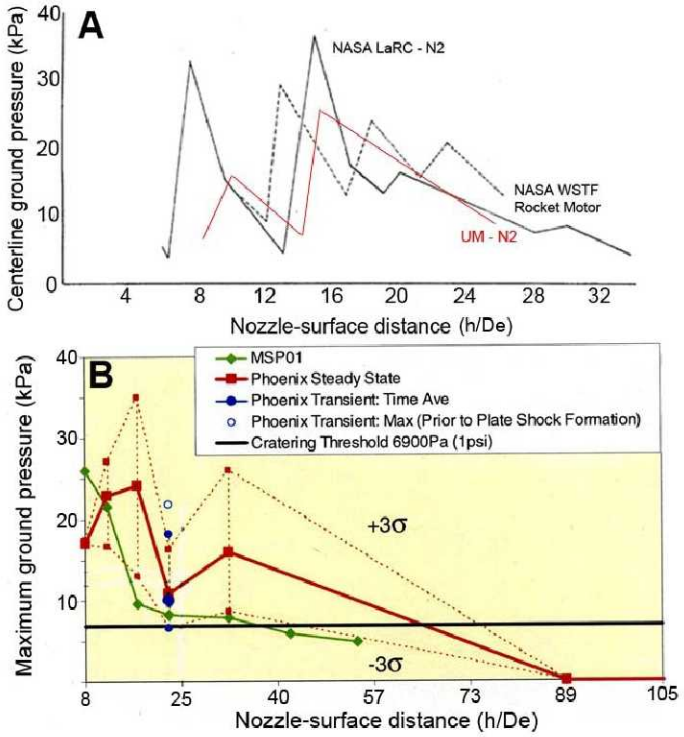


Figure 19. High variability of ground pressure vs. altitude profiles due to shock wave interactions. (A) Limited experimental results (red profile) compared to NASA WSTF and NASA LaRC studies using a single nozzle[x]; (B) Numerical result for full-scale Phoenix REM plume interactions at both steady state and transient conditions. Green curve - earlier numerical solution in support of the Mars Surveyor Program (MSP)[26].

According to Mehta et al [2010], there are five main mechanisms that lead to site-alteration and dust lifting due to plume interactions: (a) bearing capacity failure; (b) viscous erosion; (c) diffused gas erosion; (d) diffusion-driven flow and (e) diffusive gas explosive erosion. Through extensively developed scaling laws which address these five mechanisms, we can properly scale earth-gravity based tests for Mars conditions. Diffusive gas explosive erosion played a significant role in site-alteration and dust lifting due to Phoenix's pulsed thrust impact on the surface[36]. Due to the importance of understanding ground pressure profiles of thruster plume interactions, further studies were conducted in support NASA's new Mars mission.

The main parameter that is used to determine the extent of jet-induced soil erosion is the surface pressure profile of the impinging jet or rocket plume[36]. Soil pore pressure and soil properties are directly dependent on the surface pressure. However, this investigation shows that along with surface pressure magnitude and spatial profiles, the temporal pressure profile is also a critical parameter in determining the

flow physics of the exhaust gas within the granular media. To simulate surface pressure profiles, it is important to accurately simulate both the thruster inlet stagnation pressure and the atmospheric pressure environments of planetary bodies.

## SUMMARY AND CONCLUSIONS

This research investigation was ultimately undertaken to assess landing site alteration due to rocket plume impingement during spacecraft landings. The first approach, presented here, is to provide insight into plume shock structure and dynamics and their effect on ground pressure profiles. From our extensive numerical and experimental analyses, we show that moderately underexpanded jets (*e* between two and five) demonstrate collimated shock structures, compact radial pressure footprints, large supersonic core lengths, plate shock dynamics and maximum pressure loads. For *e* less than 2 and greater than 10, we illustrate a significant decline in the ground pressure loads by a factor of four with large Gaussian pressure footprints which is mainly attributed to large changes in the plume shock structure. We show that the plate shock dynamics is responsible for the following effects at the surface: increases the pressure gradients, fluctuations and average magnitudes and develops pressure asymmetry and overpressures. Therefore there is sensitivity in both shock structure and ground pressure dynamics due to both the jet expansion ratio and Strouhal number (pulsed or steady). Most importantly, the flow dynamic studies at Mars atmosphere (*e* ~2-5) show that rocket plumes possess large collimated shock cells greater than ~10*d* and generate maximum ground pressure load with respect to either lunar or terrestrial atmospheric regimes. Hence, extensive numerical and experimental investigations of plume interactions with large variations in the scaling parameters defined in Table 1 are needed to reduce mission risk associated with landing spacecrafts on Mars.

We observe good agreement (within 25%) between measurements and numerical solutions for both subscale REM and MLE nozzle plumes at various altitudes. This provides a comparison with the numerical solvers as well as provides insight to the flow physics occurring at the surface. We also observe relatively good agreement in shock structure and ground pressure dynamics between subscale and full-scale systems. Most importantly, these results show that the scaling laws developed can simulate the ground interaction physics due to rocket exhaust plumes.

The main focus of this research is to provide insight into plume-surface interactions and to demonstrate the importance of modeling and testing of these complex flow physics. This is used to provide accurate landing environment data to minimize potential hazards during spacecraft landings on planetary bodies.

## REFERENCES


1. Lamont, P. J., and B. L. Hunt (1980), The impingement of underexpanded axisymetrical jets on perpendicular and inclined flat plates, *J. Fluid Mechanics*, 100, 471- 475.

2. Fujii K et al (2002), Visualization of jet flows over a plate by pressure-sensitive paint experiments and comparison with CFD, Annals of the New York Academy of Sciences, Volume 972.

3. Hunt, JCR (1991), Industrial and Environmental Fluid Mechanics, *Ann Rev. of Fluid Mech.,* 23, 1-42.

4. Vergin, M.I. et al. (2008), Analysis of the 3-D shape of the terrestrial bow shock by interball/magion 4 observations, *Advances in Space Research*, 28, 45-55.

5. Mehta, R.C. (2008), Computations of flow field over Apollo and OPEX reentry modules at high speed, *Indian J. of Eng. & Materials*, 15, 30-40.

6. Henderson, B., et al. (2005), An experimental study of the oscillatory flow structure of tone-producing supersonic impinging jets, *J.Fluid Mechanics,* 542, 115-137.

7. Carling, J. C., and B. L. Hunt (1974), The near wall jet of a normally impinging, uniform axisymmetric, supersonic jet, *J. Fluid Mechanics,* 66, 11-19.

8. Scroggs, S.D and G.S. Settles (1996), An experimental study of supersonic microjets, *Experiments in Fluids*, 21, 401- 409.

9. Krothopalli. A., E. Rajkuperan, R. Alvi, and L. Lourenco (1999), Flow field and noise characteristics of a supersonic impinging jet, *J. Fluid Mechanics,* 392*,* 174-188.

10. Clark, L. V. (1970), Effect of retrorocket cant angle on ground erosion – a scaled Viking study, NASA Technical Memorandum. NASA TM X-2075, NASA Langley Research Center.

11. Roberts, B., et al. (1982), Plume base flow simulation technology, NASA TR – 19820023542, NASA Johnson Space and Marshall Space Flight Centers.

12. Sutton, G.P. and O. Biblarz (2001), *Rocket Propulsion Elements*, 7th edition , John Wiley & Sons Pub., New York.

13. Inman, J.A., P.M. Danehy, R.J. Nowak and D.W. Alderfer (2008) Fluorescence imaging study of impinging underexpanded jets, 46th AIAA Aerospace Sciences Meet., AIAA 2008-619.

14. Hagermann and Frey (2007), Shock pattern in the plume of rocket nozzles: needs for design consideration, *Shock Waves*, 17,6.

15. Donaldson, C. D., et al. (1971), A study of free jet impingement part 2: free jet turbulent structure and impingement heat transfer, *J. Fluid Mechanics,* 45*,* 477-512.

16. Stitt, L.E. (1963), Interaction of highly underexpanded jets with simulated lunar surfaces, NASA-TN-D-1095, NASA Glenn Research Center, Cleveland, OH.

17. Schichting, H. and K. Gersten (2001), Boundary Layer Theory, Springer: New York

18. Anderson, J.D. (2008) Modern Compressible Flow, McGraw-Hill Publishing, New York

19. Van Norman, J. W. and L. Novak (2009), CFD support of MSL MLE plume simulations. NASA Contractor Report, No. NNL04AA03Z.

20. Land, N., and H. Scholl (1966), Scaled LEM jet erosion tests, NASA Langley Working Papers, LWP–252, NASA Langley Research Center.

21. Clark, L., and W. Conner (1969a), Exploratory study of scaled experiments to investigate site alteration problems for Martian soft-lander spacecraft, NASA LWP-765, NASA Langley Research Center, Hampton, VA.

22. Choutapalli, I., A. Krothapalli and J.H. Arakeri (2009) An experimental study of an axisymmetric turbulent pulsed air jet, *J. of Fluid Mech.* 631, 23-63

23. Desai, P. N. J.L. Prince, E.M. Queen, J.R. Cruz and M.R. Grover (2008), Entry, Descent and Landing Performance of the Mars Phoenix Lander, AIAA/AAS Astrodyn.Conf,7346.

24. Sengupta, A., et al. (2009), Mars Landing Engine Plume Impingement Environment of the Mars Science Laboratory, IEEE/AIAA Aerospace Conf., 1349.

25. Romine, G. L., et al. (1973), Site alteration effects from thruster exhaust impingement during a simulated Viking Mars landing: nozzle development and physical site alteration, NASA Langley Contractor Report, CR-2252, Martin Marrieta Co.

26. Huseman, P. G. and J. Bomba (2000), CFD Analysis of Terminal Descent Plume Impingement for Mars Landers, AIAA Thermophysics Conf., 2000-2501.

27. Buning, P.G., W.M. Chan, K.Z. Renze, D.L. Sondak, I.-T. Chiu, J.P. Slotnick (1993) *OVERFLOW User's Manual, Version 1.6ab,* NASA Ames Research Center, Moffett Field, CA, Jan.

28. Nichols, R.H. (2000), Turbulence Models and Their Application to Complex Flows, University of Alabama at Birmingham, Rev. 3.0.

29. Walters, R. W., P. Cinnella, and D.C. Slack (1993), Characteristic-Based Algorithms for Flows in Thermo-Chemical Non-Equilibrium, *AIAA J.* **30**, 1304-1313

30. Van Leer, B. (1982). Flux-vector splitting for the Euler equations, in *Lecture Notes in Physics*. 170. Springer, Berlin. pp. 507-512.

31. Gulick, D.S. (2006), Phoenix Mars Lander Descent Thruster Plume/Ground Interaction Assessment, WS-06-002 Lockheed Martin Interoffice Memo, Lockheed Martin Space Systems, Denver.

32. Papp, J.L. and K.N. Ghia (1998). Study of turbulent compressible mixing layers using two-models including RNG k-ε model. AIAA paper 98-0320.

33. E. Shimshi, G. Ben-dor, and A. Levy (2009), A. Viscous simulation of shock-reflection hysteresis in over-expanded planar nozzles. *J. of Fluid Mech*., 635, 189-206.

34. Stitt and Latto (1963), Highly underexpanded exhaust jets against adjacent surfaces, NASA Technical Report - 7542

35. Menikoff, R. and B.J. Plohr (1989) The Riemann problem for real materials, *Rev.Mod. Physics*, 61, 75-130.

36. Mehta, M., et al. (2011), Explosive erosion during the Phoenix landing exposes subsurface water on Mars, *Icarus*, 211, 1.

37. White F.M. (1991), Viscous Fluid Flow, McGraw-Hill Publishing: New York.